Improving Australian Rainfall Prediction Using Sea Surface Salinity

Saurabh Rathore,[a,b] Nathaniel L. Bindoff,[a,c,d,e] Caroline C. Ummenhofer,[c,f] Helen E. Phillips,[a,c] Ming Feng,[g,h] and Mayank Mishra[i]

[a] *Institute for Marine and Antarctic Studies, University of Tasmania, Hobart, Tasmania, Australia*
[b] *ARC Centre of Excellence for Climate System Science, Hobart, Tasmania, Australia*
[c] *ARC Centre of Excellence for Climate Extremes, Sydney, New South Wales, Australia*
[d] *CSIRO Oceans and Atmosphere, Hobart, Tasmania, Australia*
[e] *Australian Antarctic Program Partnership, Hobart, Tasmania, Australia*
[f] *Woods Hole Oceanographic Institution, Woods Hole, Massachusetts*
[g] *CSIRO Oceans and Atmosphere, Indian Ocean Marine Research Centre, Crawley, Western Australia, Australia*
[h] *Centre for Southern Hemisphere Oceans Research, CSIRO, Hobart, Tasmania, Australia*
[i] *Centre for Oceans, Rivers, Atmosphere and Land Sciences, Indian Institute of Technology Kharagpur, Kharagpur, India*

(Manuscript received 6 August 2020, in final form 22 December 2020)

ABSTRACT: This study uses sea surface salinity (SSS) as an additional precursor for improving the prediction of summer [December–February (DJF)] rainfall over northeastern Australia. From a singular value decomposition between SSS of prior seasons and DJF rainfall, we note that SSS of the Indo-Pacific warm pool region [SSSP (150°E–165°W and 10°S–10°N) and SSSI (50°–95°E and 10°S–10°N)] covaries with Australian rainfall, particularly in the northeast region. Composite analysis that is based on high or low SSS events in the SSSP and SSSI regions is performed to understand the physical links between the SSS and the atmospheric moisture originating from the regions of anomalously high or low, respectively, SSS and precipitation over Australia. The composites show the signature of co-occurring La Niña and negative Indian Ocean dipole with anomalously wet conditions over Australia and conversely show the signature of co-occurring El Niño and positive Indian Ocean dipole with anomalously dry conditions there. During the high SSS events of the SSSP and SSSI regions, the convergence of incoming moisture flux results in anomalously wet conditions over Australia with a positive soil moisture anomaly. Conversely, during the low SSS events of the SSSP and SSSI regions, the divergence of incoming moisture flux results in anomalously dry conditions over Australia with a negative soil moisture anomaly. We show from the random-forest regression analysis that the local soil moisture, El Niño–Southern Oscillation (ENSO), and SSSP are the most important precursors for the northeast Australian rainfall whereas for the Brisbane region ENSO, SSSP, and the Indian Ocean dipole are the most important. The prediction of Australian rainfall using random-forest regression shows an improvement by including SSS from the prior season. This evidence suggests that sustained observations of SSS can improve the monitoring of the Australian regional hydrological cycle.

KEYWORDS: ENSO; Flood events; Hydrologic cycle; Machine learning; Rainfall; Salinity; Seasonal forecasting; Soil moisture

1. Introduction

Various climate drivers that include oceanic and atmospheric modes, such as El Niño–Southern Oscillation (ENSO), the Indian Ocean dipole (IOD), the southern annular mode (SAM), and others, profoundly influence Australian rainfall not only on interannual time scales (Risbey et al. 2009; Hendon et al. 2014; Lim and Hendon 2015) but also on decadal time scales (Power et al. 1998, 1999, 2006). Among these variations, ENSO and IOD have, perhaps, the most impact (McBride and Nicholls 1983; Ashok et al. 2003; Risbey et al. 2009; Ummenhofer et al. 2009; Cai et al. 2012) with implications for Australia's ecosystems and socioeconomic prospects (NCCARF 2012; Holmes 2012; Hayes and Goonetilleke 2013; Yuan and Yamagata 2015). Yet there is still a need to improve the prediction of Australian rainfall through the inclusion of additional variables (such as salinity and soil moisture) to help anticipate such impacts.

Our previous study (Rathore et al. 2020) shows that sea surface salinity (SSS) is linked with Australian rainfall via atmospheric moisture transport. The anomalous positive and negative SSS of the Indo-Pacific warm pool appears prior to the peak of ENSO and IOD events and is accompanied by convergence and divergence of atmospheric moisture transport. Also the use of SSS of the Atlantic Ocean and tropical northwest Pacific Ocean for the prediction of rainfall has been demonstrated in Li et al. (2016a,b) and Chen et al. (2019). It is shown that the moisture originating from the ocean surface leaves an imprint on the SSS that in turn can be used as a precursor for rainfall over adjacent land areas (Li et al. 2016a,b; Chen et al. 2019). Here, we use this relationship between the SSS and atmospheric moisture to predict the rainfall over Australia, which has not been previously investigated. In conjunction with Rathore et al. (2020), this study shows the use of SSS as an additional precursor along with local soil moisture, ENSO, and IOD indices to improve the prediction of Australian rainfall. The links between the SSS and rainfall over land cannot be interpreted as SSS driving or shaping rainfall over land in the same way that ENSO, a remote driver, and soil moisture, a local driver, do. The persistent signature of ENSO evolution and the

Corresponding author: Saurabh Rathore, saurabh.rathore@utas.edu.au

DOI: 10.1175/JCLI-D-20-0625.1

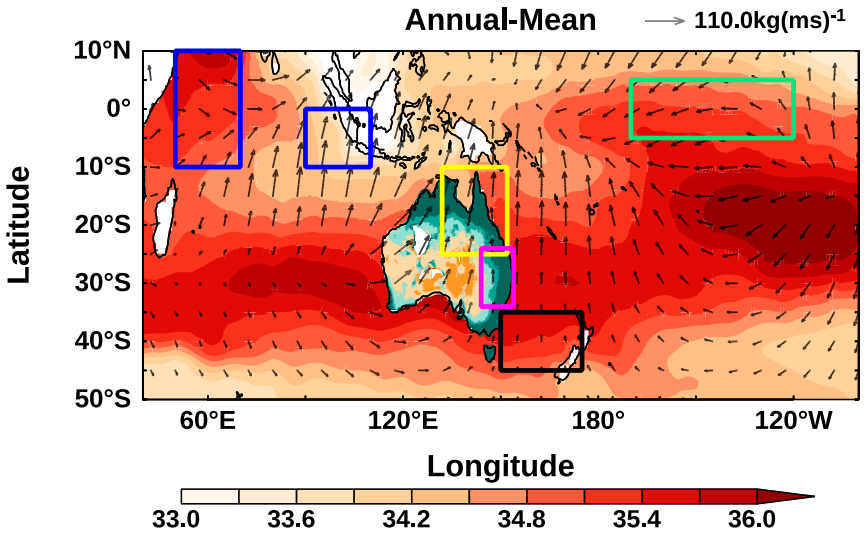

FIG. 1. Annual mean of SSS for the study area overlaid with the outlined boxes for the DMI (blue), Niño-3.4 index (green), region of northeastern Australia (yellow), region of Brisbane (magenta), and Tasman Sea region (black), with vectors of moisture transport, i.e., divergent component of moisture flux and the Australian precipitation, where brown indicates low rainfall and green indicates high.

response of soil moisture to the convergence and divergence in prior seasons drive the precipitation over land in the later season (Hendon et al. 1989; Timbal et al. 2002; Evans et al. 2011). The convergence/divergence of moisture, which is also associated with the evolution of ENSO, is imprinted on SSS in the prior season before ENSO peaks (Rathore et al. 2020). Hence, this study is about testing the use of SSS as an additional precursor that can be used along with other remote and local drivers to improve the prediction of Australian rainfall.

The study's application is demonstrated for the broader Brisbane region because it encountered Australia's severe precipitation anomalies during 1973/74 and 2010/11 years (Ummenhofer et al. 2015). Recent records (NCCARF 2012; Holmes 2012; Hayes and Goonetilleke 2013) show that the financial and human loss due to the flooding event associated with the extreme hydroclimatic conditions of 2010/11 was estimated to be around $2 billion and 35 deaths. The flooding events in both the 1973/74 and 2010/11 years were associated with co-occurring La Niña and negative IOD (nIOD), which generally bring anomalously high rainfall over Australia's northeast region (Evans and Boyer-Souchet 2012; Zhu 2018; Rathore et al. 2020).

The paper is organized as follows. Section 2 provides the method and datasets, respectively, used in this study. Sections 3–6 focus on the links between SSS and Australian rainfall with physical mechanisms and the application of SSS for the prediction of Australian rainfall over the northeast and broader Brisbane region. Section 7 is the discussion of the results, and section 8 is conclusions of the study.

2. Data and method

a. Data

Our study is focused on the Indo-Pacific region and is bounded by 40°E–100°W and 50°S–10°N with the regions of IOD and ENSO defined by the (two) blue and green box, respectively, in Fig. 1. Monthly means of various oceanic and atmospheric parameters from observations and reanalysis are used in this study from 1961 to 2017. For climate variability measures, we use the Niño-3.4 index for ENSO and the dipole mode index (DMI) for IOD. The ENSO index is the area-averaged SST anomaly in the equatorial Pacific region bounded by 5°S–5°N and 170°–120°W (Fig. 1, green box) and is based on the monthly time series of ERSSTv5 (Huang et al. 2017). The DMI is based on Saji et al. (1999) and is computed as the difference of spatially averaged SST anomaly between the western equatorial (50°–70°E, 10°S–10°N; Fig. 1, big blue-outlined box) and the southeastern equatorial (90°–110°E, 10°S–0°; Fig. 1, small blue-outlined box) Indian Ocean. Both of these indices were linearly detrended to enable a focus on interseasonal-to-interannual climate variability. We have used the monthly time series of these two indices from online sources (ENSO: https://origin.cpc.ncep.noaa.gov/products/analysis_monitoring/ensostuff/ONI_v5.php DMI: https://www.esrl.noaa.gov/psd/gcos_wgsp/Timeseries/DMI/). We have used three different products for the monthly means of SSS data. The SSS data include two products from Hadley Centre subsurface objective analyses (EN 4.2.1; Good et al. 2013) that are bias corrected following the approaches of Levitus et al. (2009) and Gouretski and Reseghetti (2010). In the equations below, data from these two sources are labeled as L09 and G10, respectively. The third SSS product is the Ocean Reanalysis System 4 (ORAS4) (Balmaseda et al. 2013) from the European Centre for Medium-Range Weather Forecasts (ECMWF).

EN4 data (Good et al. 2013) are produced by incorporating the World Ocean Database (WOD) as a main data source used for reconstruction of temperature and salinity fields along with the Coriolis dataset for Reanalysis (CORA). Data from the

Global Temperature and Salinity Profile program (GTSPP) from 1990 onward and Argo data from 2000 onward were also included in EN4. The quality-controlled data are used to produce a monthly objective analysis of the temperature and salinity from all types of ocean profiling instruments. By persisting anomalies through to the next month, a forecast of the ocean state is produced, and this is used in the quality control of the following month of data and as the background to the next month's analysis (Good et al. 2013).

For ORAS4 (Mogensen et al. 2012), data are assimilated using NEMOVAR, which is a variational data assimilation software for the NEMO ocean model. ORAS4 assimilates temperature and salinity profiles from the quality-controlled EN3 dataset, which includes data from expandable bathythermographs (XBT), conductivity–temperature–depth sensors (CTD), Argo, and moorings for the period of 1957–2009. From 2010, real-time data from the Global Telecommunications System (GTS) are used.

Usually, the assimilation of ocean data brings the state closer to reality, but only in the presence of enough observations. In the early 1960s the surface ocean is more sparsely sampled in SSS datasets and is therefore the most unreliable period in the full time series analyzed here. To reduce the uncertainty in the ECMWF's ORAS4 product, an ensemble generation strategy is used with time-varying fluxes and assimilating temperature and salinity, for the period from 1958 to 1980, which improves the fit to the temperature and salinity profiles (Balmaseda et al. 2013). We have used the ensemble mean of the three SSS datasets, as mentioned above. The ensemble mean approach results in the mean smoother field with a small standard error. This approach is consistent with using as much of the data on SSS as is available across a suite of products (which use different methods). Furthermore, the use of the machine-learning approach with random selection of the independent learning samples generates a robust prediction of the testing data by minimizing the underlying uncertainties in the data across the entire time record. However, the records after 1990 are the most well sampled.

Likewise, we have used the ensemble mean of three different products for the monthly terrestrial precipitation over Australia: the Australian Water Availability Project (AWAP) (Raupach et al. 2009), NOAA's National Weather Service/Climate Prediction Center (CPC) (Chen et al. 2002), and the Climate Research Unit (CRU) (New et al. 2000; Mitchell and Jones 2005).

We also used monthly means of specific humidity and horizontal winds between 1000 and 500 hPa from NCEP–NCAR Reanalysis 1 (Kalnay et al. 1996). However, it is important to mention that the specific humidity and horizontal winds from the NCEP–NCAR Reanalysis 1 are the averages of the instantaneous values at every 6 h over the averaging period (1 month). Monthly SST data are from HadISST1 (Rayner et al. 2003), and monthly means of soil moisture data are from NOAA's CPC Soil Moisture dataset (Fan and van den Dool 2004). We focus on seasonal time scales, which are prone to be less noisy than the higher-frequency time scales. Moreover, the lack of availability of submonthly data is also one of the constraints, so we used the monthly data for the seasonal analysis.

b. Methods

Monthly anomalies are computed for each dataset by removing their respective monthly climatology and then detrending the anomaly time series to remove long-term trends. The three different time series of SSS anomaly and rainfall anomaly are averaged, as shown in Eqs. (1) and (2) respectively, to eliminate the biases from the different interpolation and reanalysis techniques:

$$\mathrm{SSS} = \frac{\mathrm{SSS}_{\mathrm{ORAS4}} + \mathrm{SSS}_{\mathrm{G10}} + \mathrm{SSS}_{\mathrm{L09}}}{3} \quad \text{and} \tag{1}$$

$$\mathrm{rain} = \frac{\mathrm{rain}_{\mathrm{AWAP}} + \mathrm{rain}_{\mathrm{CPC}} + \mathrm{rain}_{\mathrm{CRU}}}{3}. \tag{2}$$

The moisture flux divergence (MFD) is computed as follows:

$$\mathrm{MFD} = \left(\frac{1}{g}\right)\nabla \cdot \int_0^{P_s} q\mathbf{V}\, dp \;\cong\; (E - P), \tag{3}$$

where g is the gravitational acceleration (9.8 m s^{-2}), q is specific humidity (g kg^{-1}), $\mathbf{V}$ is horizontal wind velocity (m s^{-1}), E is evaporation, and P is precipitation. Moisture flux $q\mathbf{V}$ is computed at each pressure level of the reanalysis and then integrated from the surface (1000 hPa) to 500 hPa. The upper limit of integration is taken as 500 hPa, because the majority of the moisture in the atmosphere is concentrated below this level (Zhou and Yu 2005; Li et al. 2013; Seager and Henderson 2013; Li et al. 2016a). The divergent component of moisture flux (MF) is computed by solving Poisson equations (Lynch 1988), and this component shows the pathways of moisture transport. Seasonal averages of July–September (JAS), September–November (SON), and December–February (DJF) are computed for each detrended and deseasonalized time series.

We used singular value decomposition (SVD) (Wallace et al. 1992) to assess the covariability between SSS and Australian rainfall. The SSS anomalies within the region 40°E–100°W and 50°S–10°N are included in the analysis, and the rainfall anomaly is over the Australian land area. This analysis helps to identify the regions of SSS anomaly in the ocean that covary with the rainfall anomalies over the Australian landmass. The regions of SSS [SSSP (150°E–165°W and 10°S–10°N) and SSSI (50°–95°E and 10°S–10°N); red-outlined boxes in Figs. 2a,d,g] and rainfall [northeastern Australia (132°–152°E and 25°–10°S; red-outlined box in Figs. 2b,e,h) and Brisbane (144°–154°E and 34°–24°S; blue-outlined box in Figs. 2b,e,h] are based on the pattern that we obtained from the SVD analysis. We then made the box average of SSS over the selected regions in the western equatorial Pacific (SSSP) and eastern equatorial Indian Ocean (SSSI). Similarly, the region of northeastern Australia with the prominent pattern in SVD analysis is used to generate the rainfall time series. For composite analysis, we selected the high and low SSS anomaly events in the top and bottom deciles of the SSS anomaly of those oceanic regions that covary with Australian rainfall.

The significance test for the composite analysis is estimated by using a Monte Carlo simulation with replacement. The use of Monte Carlo simulation to test the significance of composite

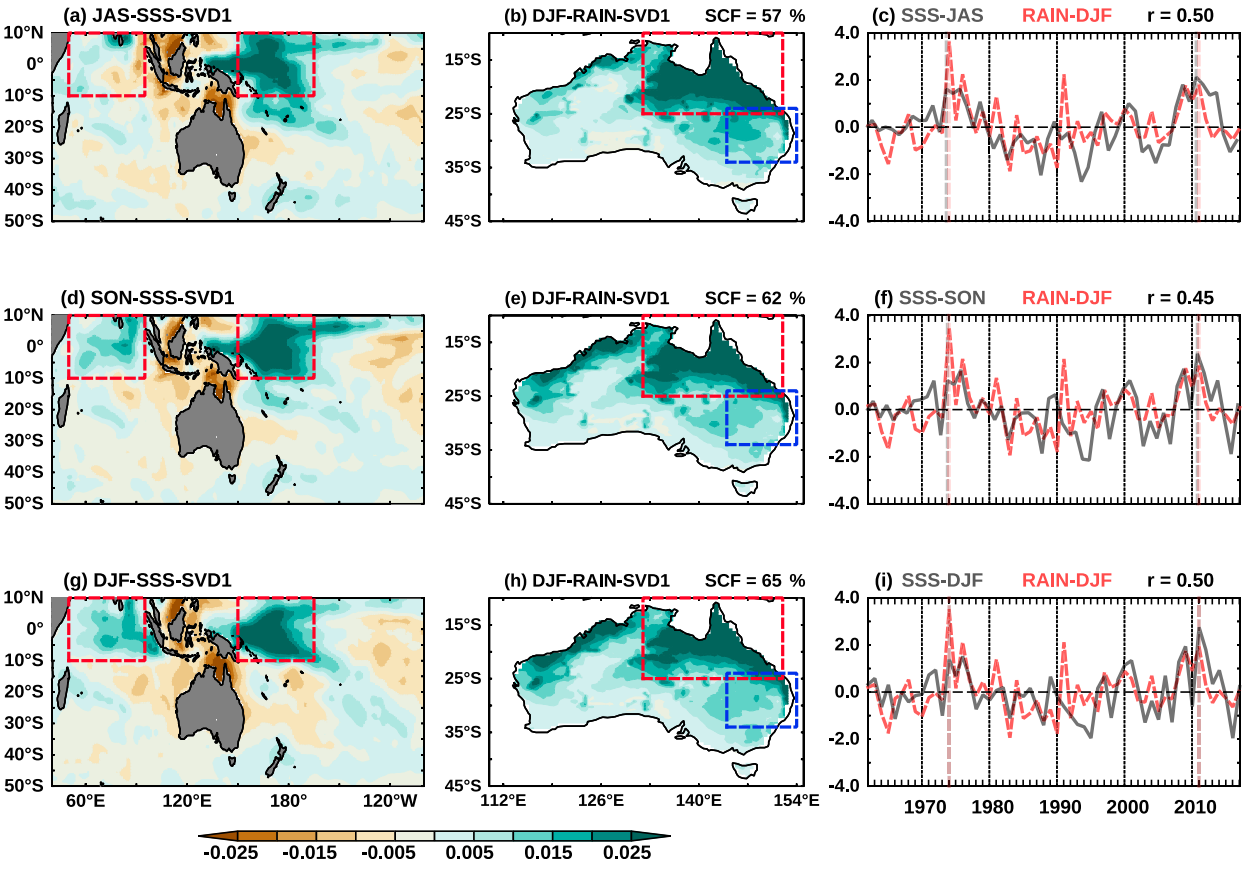

FIG. 2. First mode of joint SVD analysis of SSS anomaly during (a) JAS, (d) SON, and (g) DJF associated with the DJF rainfall; DJF rainfall anomaly associated with the SSS anomaly of (b) JAS, (e) SON, and (h) DJF; and the normalized time series associated with the first mode of SVD analysis of SSS anomaly (red) for (c) JAS, (f) SON, and (i) DJF and Australian rainfall anomaly (gray). The explained variance by SVD analysis of SSS anomaly and rainfall anomaly is represented by square covariance fraction (SCF), and the correlation coefficient between the associated normalized time series is represented by r, which is significant at 95% from a two-tailed Student's t test. The SSSI region (left red-outlined box) of the Indian Ocean and SSSP region (right red-outlined box) region of Pacific Ocean are shown in (a), (d), and (g); northeastern Australia (red-outlined box) and the Brisbane region (blue-outlined box) are shown in (b), (e), and (h).

means is demonstrated by Terray et al. (2003). The aim of using Monte Carlo simulation is to test whether the composites are significantly different from the background variability present in those data. For the usual Student's t test, the underlying assumption is that the sample years used for the composite mean are drawn independently from the population and the alternate testing hypothesis is that the composite mean is different from the population mean. It is also assumed in Student's t test that the data are distributed normally, which is not necessarily an appropriate assumption in climate research and particularly for variables like precipitation (Nicholls 2001).

To test the significance of the composite mean, the null hypothesis states that the composite mean of high and low decile years (μ_1) is the same as the composite mean of randomly selected years (μ_0). Of the total 56 events, μ_1 is estimated from the six events of each high and low decile category. In contrast, μ_0 is estimated from the composite mean of six randomly selected years, and this procedure is repeated 10 000 times to generate a Gaussian distribution of the composite mean μ_0. In summary, the hypotheses are

- null hypothesis H_o: $\mu_1 = \mu_0$ and
- alternate hypothesis H_1: $\mu_1 \neq \mu_0$.

So, the null hypothesis states that the composite mean of high and low decile years (μ_1) is the same as the composite mean of six randomly selected years (μ_0) if it lies between $\pm$(1.645 multiplied by the standard deviation of the distribution of composite mean generated by the random selection of six years for 10 000 times). This is equivalent to the 90% confidence from Student's two-tailed t test. In contrast, the alternate hypothesis puts the composite mean (μ_1) outside this bound and makes it significantly different from the background variability (μ_0).

Rathore et al. (2020) have shown that there is a link between SSS anomaly and the Australian rainfall anomaly during ENSO/IOD events. These events are the prominent modes in the tropical Indo-Pacific Ocean that have a profound influence on Australian rainfall (Ashok et al. 2003; Cai et al. 2009; Ummenhofer et al. 2009, 2011; Taschetto et al. 2011; King et al. 2015) and SSS (Delcroix et al. 1996; Grunseich et al. 2011;

Singh and Delcroix 2011). Moreover, the east Australian region from north to south is a vulnerable region and more prone to flooding events (Halgamuge and Nirmalathas 2017; Hu et al. 2018). Hence, it is necessary to improve the prediction of DJF rainfall over Australia.

For the prediction, we have used random-forest regression analysis. The random-forest regression is a nonlinear machine-learning algorithm, developed by Breiman (2001) based on classification and regression trees (CART) analysis. This machine-learning algorithm takes an ensemble learning approach, that is, the use of multiple decision trees for the prediction (Breiman 2001). If we use a single decision tree, then there is a high chance of overfitting due to the decision tree's sensitivity to data variations. However, increasing the number of decision trees with random selection of training data reduces the overfitting. The final prediction is the ensemble average of the predictions generated by each decision tree and hence it is considered to be an ensemble learning approach. This method accounts for the relationship between the predictors themselves and their relationship to the predictand.

The advantage of using a random-forest technique over traditional linear regression is that the random-forest approach assumes neither linearity nor that the data are drawn from a particular distribution (Firth et al. 2005). The ensemble learning approach of the random-forest algorithm can improve overall prediction accuracy and avoids overfitting that commonly occurs due to highly correlated predictors (Breiman 2001; Pal et al. 2020). In contrast to the random-forest regression, which is a nonparametric approach, simple/multiple linear regression is a global parametric model and applies a single predictive formula to the entire data time series (Chen et al. 2012; Noi et al. 2017). Despite having limited capability to explicitly account for the underlying processes, the machine-learning-based predictions generally have shown good skill in forecasting events (Pal et al. 2020).

As we have mentioned, random-forest regression is an ensemble learning approach in which a large number of decision trees are grown to build a forest. Multiple trees can be constructed from randomly selected training samples. For the prediction of DJF rainfall over northeastern Australia (132°–152°E and 25°–10°S) using random-forest regression, we used two indices of SSS anomaly [SSSP (150°E–165°W and 10°S–10°N), and SSSI (50°–95°E and 10°S–10°N)], two indices that are based on SST anomaly (Niño-3.4 index and DMI), and the local soil moisture of northeastern Australia.

In random-forest regression, we train the model with the spatially averaged rainfall anomaly of northeastern Australia, the region marked by the yellow-outlined box in Fig. 1 and red-outlined box in Figs. 2b,e,h, spatially averaged SSS anomaly from the western Pacific (SSSP) and Indian Ocean (SSSI) over the region marked by red-outlined boxes in Figs. 2a,d,g, and spatially averaged soil moisture over northeastern Australia, Niño-3.4, and the DMI. The rainfall anomaly index is seasonally averaged for DJF, whereas SSSP, SSSI, soil moisture, Niño-3.4, and the DMI are seasonally averaged over JAS and SON. After constructing these indices, we used the DJF rainfall anomaly as predictand and JAS and SON indices of SSSP, SSSI, soil moisture, Niño-3.4 index, and DMI as predictors.

In this study we have used 50% of the data that are randomly selected for training and to develop the decision tree model. The remaining 50% of the data that were withheld are used to test the model to obtain the unbiased estimates of the regression error and the importance of the variables used for constructing the regression tree. The coefficient of determination is used to evaluate the performance of the model; that is, $R^2 = 1 - (V_{\text{residual}}/V_{\text{total}})$, where R^2 is the variance explained by the random-forest regression model. Also, $V_{\text{residual}} = \sum_{k=1}^{n}[f(X)_k - P_k]^2$ is the variance that cannot be explained by the random-forest regression model, $f(X)$ is the predicted value from random-forest regression, and P_k is the observed rainfall for $k = 1, 2 \ldots, n$ years; $V_{\text{total}} = \sum_{k=1}^{n}(P_k - \overline{P})^2$ is the total variance of the observed rainfall, and $\overline{P}$ is the overall average of the observed rainfall.

This prediction assessment was run 300 times, on each iteration the number of trees was increased by 5, and R^2 was averaged over these iterations. For the training of each decision tree, we have randomly selected 50% of data (i.e., predictors and target variable) and the remaining 50% of data are used for testing (i.e., predicting the target variable from the trained decision tree to get the R^2 value). The predictions from each decision tree are then averaged across all decision trees to obtain the overall model score (R^2). For the prediction of an entire time series, the ensemble average of the coefficients is used (i.e., the coefficients that are obtained during the training). So, the final predicted target variable is obtained for each year by averaging the ensemble of 1500 predictions obtained from 1500 decision trees. We have tested this algorithm by changing the number of iterations from 300 to 200 and 500, and the results were unchanged. A similar analysis has been used for predicting rainfall over different parts of the world, such as the Sahel, the U.S. Midwest, and the East Asian monsoon region over China (Li et al. 2016b,a; Chen et al. 2019).

We have also assessed each index's importance for its contribution to prediction of rainfall, which is also known as feature importance. For the assessment of each index's importance, we have used the ''permutation feature'' importance method (Altmann et al. 2010). This method is defined as the decrease in a model score R^2 when a single feature is shuffled randomly, and all other features remain unchanged. The random shuffling of the feature (predictor) breaks its relationship to the response variable (predictand). Thus, the drop in the model score indicates how much the model depends on this feature. We applied this feature importance method on the testing data (withheld or unseen data) rather than training data, which reduces the risk of overfitting and biases that favor high cardinality features in the training data. Moreover, the permutation importance function is quite useful because it accounts for the nonlinearity within the predictors. To get the importance score, we randomly shuffled each index 1500 times using the permutation feature importance method.

Hence the advantage of the random-forest regression and permutation feature importance analysis is that it explicitly tests and reduces the risk of overfitting by considering the nonlinearity and colinearity of the predictors and predictand as shown by many studies (Breiman 2001; Altmann et al. 2010; Chen et al. 2012; Li et al. 2016a,b; Noi et al. 2017; Ghosh and

TABLE 1. Years of high and low SSS events for the SSSP and SSSI regions.

	High SSS years	Low SSS years
SSSP region (150°–165°W and 10°S–10°N)	1971, 1975, 2007, 2008, 2010, and 2011	1972, 1987, 1993, 1994, 2002, and 2015
SSSI region (50°–95°E and 10°S–10°N)	1969, 1976, 1981, 1986, 2001, and 2010	1962, 1963, 1967, 1968, 1978, and 1997

Behera 2018; Chen et al. 2019; Das and Pandey 2019; Pal et al. 2020).

Similarly, the random-forest regression analysis is also applied for the case study of the broader region that surrounds Brisbane (144°–154°E, 34°–24°S), delineated in Fig. 1 (magenta-outlined box) and Fig. 2 (blue-outlined box) of 10° × 10° spatial scale. The delineated region is sufficiently large to perform a test case for the regional analysis. All the predictors used for the Brisbane region analysis are the same as in the northeastern Australia analysis except the local soil moisture, which is for the Brisbane region.

3. Singular value decomposition

SVD analysis of multiple fields is a technique to investigate the fields that covary spatially and temporally (i.e., they seem to have some degree of correlation). A recent study from Rathore et al. (2020) shows that the variability of SSS in the Indo-Pacific warm pool is linked to Australian rainfall anomalies via atmospheric moisture transport. Therefore, in this study, we are assessing the covariability of the SSS anomaly over the Indo-Pacific domain (Fig. 1) and the Australian rainfall anomaly.

Figure 2 shows the joint SVD analysis of the two fields (SSS anomaly during JAS, SON, and DJF and Australian rainfall anomaly during DJF). The first mode of SVD (SVD1) shows that the positive loading of JAS SSS anomaly (Fig. 2a) of the western Pacific warm pool (SSSP over 150°E–165°W, 10°S–10°N) strongly covaries with the positive loading of DJF rainfall anomaly (Fig. 2b) over northeastern Australia. However, a very weak signal of SSS anomaly is present in the Indian Ocean (SSSI over 50°–95°E, 10°S–10°N). The first mode of JAS SSS anomaly and DJF rainfall anomaly jointly explains 57% of the variance. The time series associated with the first mode of SVD (Fig. 2c) shows the covariability of JAS SSS anomaly and DJF rainfall anomaly. A significant correlation ($r = 0.50$ at $\alpha = 0.05$) exists between the time series of JAS SSS anomaly and DJF rainfall anomaly associated with the first mode of SVD. Furthermore, the signatures in JAS SSS anomaly during 1973 and 2010 covary with the heavy precipitation events over Australia in the following season of DJF.

As compared with JAS, the first mode of SVD of the SON SSS anomaly (Fig. 2d) has now developed a positive loading over the SSSI region, and a more concentrated positive loading is observed over the SSSP region with a weakening south of 10°S. This pattern of SSS anomaly during SON is plausibly associated with the development of the ENSO and IOD events (Ballabrera-Poy et al. 2002; Grunseich et al. 2011; Singh and Delcroix 2011; Kido et al. 2019).

The explained variance (Fig. 2e) corresponds to the first mode of SVD of SON SSS anomaly, and DJF rainfall anomaly is increased to 62%. This increase in the variance is plausibly due to the increased positive loading of rainfall anomaly over the northwestern coastal strip of Australia (Fig. 2e); however, our analysis is primarily concentrated on eastern Australia and other regions are outside the scope for this study. The correlation between the time series of SON SSS anomaly and DJF rainfall anomaly, which is associated with the first mode of SVD, is marginally reduced to 0.45 but still significant at $\alpha = 0.05$.

This pattern of loading in SSS anomaly and rainfall anomaly is continued from SON to the concurrent season of DJF, and the first mode of SVD of DJF SSS anomaly and DJF rainfall anomaly jointly explains 65% of the variance with a significant temporal correlation of $r = 0.50$ ($\alpha = 0.05$) between their associated time series. This analysis suggests that the SSS anomaly of the previous seasons (JAS and SON) over the region of Indo-Pacific warm pool (SSSP and SSSI) is coupled with the rainfall anomaly over northeastern Australia in the following season (DJF). Moreover, the heavy precipitation events of Australia during 1973/74 and 2010/11 are consistent with the anomalously high SSS in prior seasons (Figs. 2c,f).

4. Composite analysis based on high and low SSS anomaly events

The composite analysis is based on high and low SSS anomaly events selected as a top and bottom decile, respectively, from the spatially averaged SSSP and SSSI time series during SON. The years of high and low SSS of SSSP and SSSI region used for the composite analysis are shown in Table 1. These anomalously high and low SSS events of the SSSI and SSSP regions of the Indo-Pacific warm pool are related to the anomalously wet and dry conditions over northeastern Australia. Hence, a composite analysis is conducted to investigate the links between the ocean and atmosphere during the high and low SSS anomaly events of the SSSP and SSSI regions of the Indo-Pacific warm pool and the rainfall over Australia. These links are described in the following section.

a. Composite analysis based on high SSS anomaly events of SSSP region

The high SSS years of the SSSP region used for the composite analysis are 1971, 1975, 2007, 2008, 2010, and 2011. The composite mean of SST anomaly (Fig. 3, first column), which is based on high SSS anomaly events of the SSSP region, shows the development of La Niña in the tropical Pacific and weaker insignificant signature of nIOD in the Indian Ocean. These signatures of La Niña with weak nIOD are also present in the SSS anomaly (Fig. 3, second column) where anomalously high SSS of the SSSP region coincides with a weak and insignificant positive SSS anomaly signal in the SSSI region that is weakly intensified from JAS to DJF. These

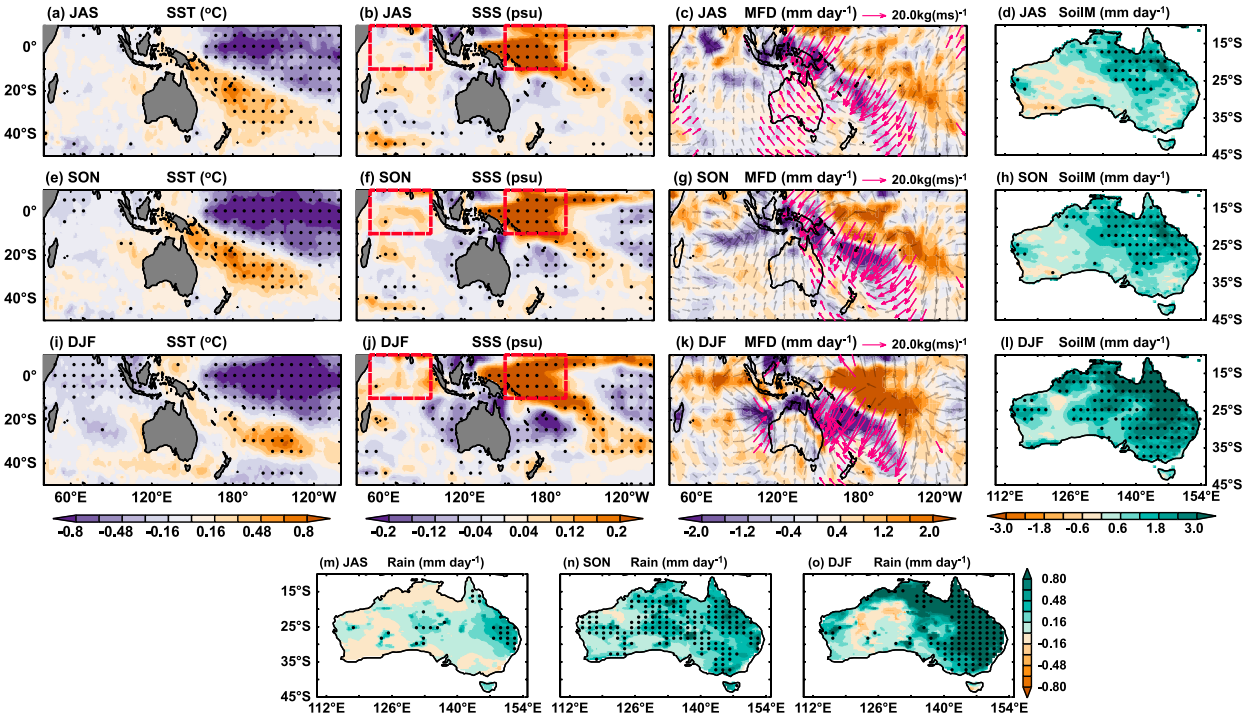

FIG. 3. Composite analysis based on high SON SSS events of the SSSP region during JAS, SON, and DJF for (a),(e),(i) SST anomaly; (b),(f),(j) SSS anomaly; (c),(g),(k) MFD anomaly (shading) overlaid by vectors of divergent component of moisture flux anomaly; (d),(h),(l) soil moisture anomaly; and (m)–(o) rainfall anomaly. Stippled regions and magenta vectors are significant at 90%.

conditions of positive SSS anomalies correspond to the evaporation of moisture from the ocean surface and the SSSP region appears to be the primary source of moisture transport over northeastern Australia. In contrast, negative SSS anomalies around the east and west coast of Australia correspond to the freshening due to precipitation (Fig. 3, second column).

The moisture flux that originates from the ocean surface coincides with the atmospheric divergence (Fig. 3, third column) over the anomalously high SSS regions of the Indo-Pacific warm pool (SSSP and SSSI). A large part of the significant moisture transport toward Australia that is primarily sourced from the SSSP region coincides with the atmospheric convergence over northeastern Australia. There are two main branches of moisture transport toward Australia during JAS (Fig. 3c): one is the direct branch from the SSSP region and the second branch is over the Tasman Sea. In the later season (SON and DJF) there are three additional branches of moisture transport emerging in which two branches are from the tropical Indian Ocean, and the third branch is from the south of Australia (Figs. 3g,k). Overall, the moisture source from the SSSP region is a significant contributor to the northeast Australian rainfall. In contrast, less moisture originates from the weakly intensified SSSI region (weak positive SSS anomalies) and converges over the ocean in the vicinity of western Australia.

The convergence of the incoming moisture transport over Australia coincides with the anomalously high soil moisture (Fig. 3, fourth column), which progressively increases from JAS to DJF. The significant positive soil moisture anomalies in northeastern Australia during JAS (Fig. 3d) get intensified and spread over a large part of the continent in the later seasons (Figs. 3h,l). This anomalous rise in soil moisture (Fig. 3, fourth column) is corroborated with anomalously wet conditions over Australia. Significant rainfall anomalies over eastern Australia during JAS (Fig. 3m) expand to a widespread wetting during SON (Fig. 3n).

Interestingly, the widespread wetting of SON retreated during DJF, and significant wetting is primarily confined to eastern Australia. It is worth mentioning that the regions of high SSS anomalies do not coincide perfectly with the regions of high MFD, which likely signifies the role of oceanic currents in advecting the SSS anomaly created by surface freshwater flux (Yu 2011; Li et al. 2016b).

b. *Composite analysis based on low SSS anomaly events of the SSSP region*

The low SSS years of the SSSP region used for the composite analysis are 1972, 1987, 1993, 1994, 2002, and 2015. The composite analysis for the low SSS events in the SSSP region is shown in Fig. 4 and is opposite in phase to the high SSS events in this region (Fig. 3). During the low SSS events in the SSSP region, signatures of co-occurring El Niño and positive IOD (pIOD) are observed in the equatorial Indian and Pacific Oceans as shown by the composite mean of SST anomaly (Fig. 4, first column). As the signatures of co-occurring El Niño and pIOD in SST get intensified from JAS to DJF, the significant salty and fresh signatures in SSS are also strengthened (Fig. 4, second column).

The salty (fresh) anomalies (Fig. 4, second column) to the north of Australia (SSSP and SSSI region) indicate the source

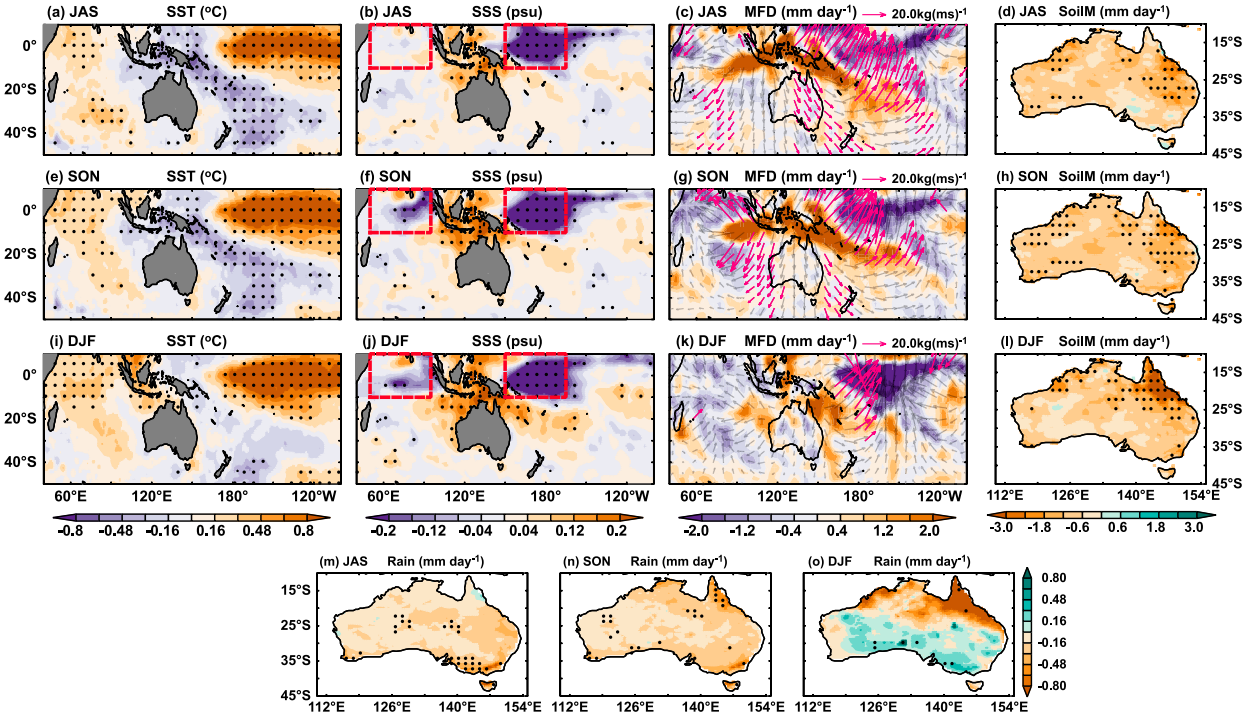

FIG. 4. As in Fig. 3, but for low SON SSS events.

(sink) region of atmospheric moisture (Fig. 4, third column). From JAS to DJF a large amount of significant moisture that originates from the source region converges over the SSSI and SSSP region in the ocean north of 10°S (Fig. 4, third column). In contrast, the amount of moisture that is directed toward Australia from the source regions coincides with the atmospheric divergence over the Australian landmass and diverges further, away from south of 10°S (Fig. 4, third column).

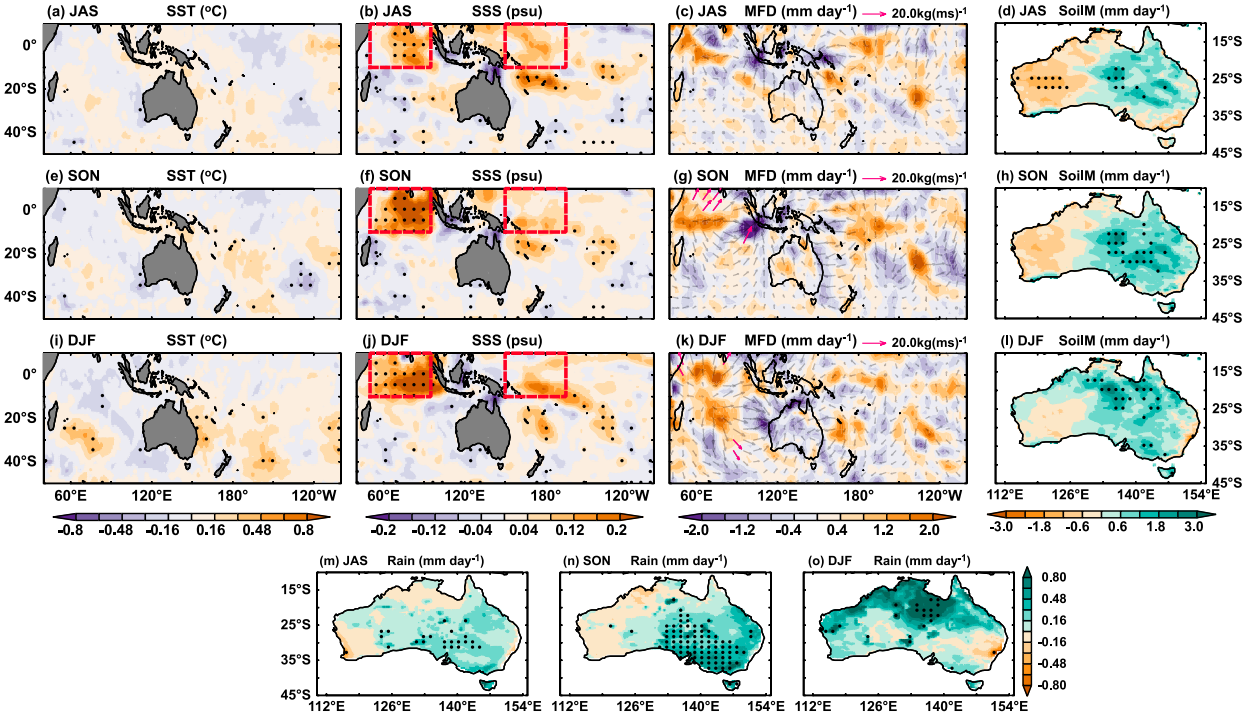

FIG. 5. As in Fig. 3, but for the SSSI region.

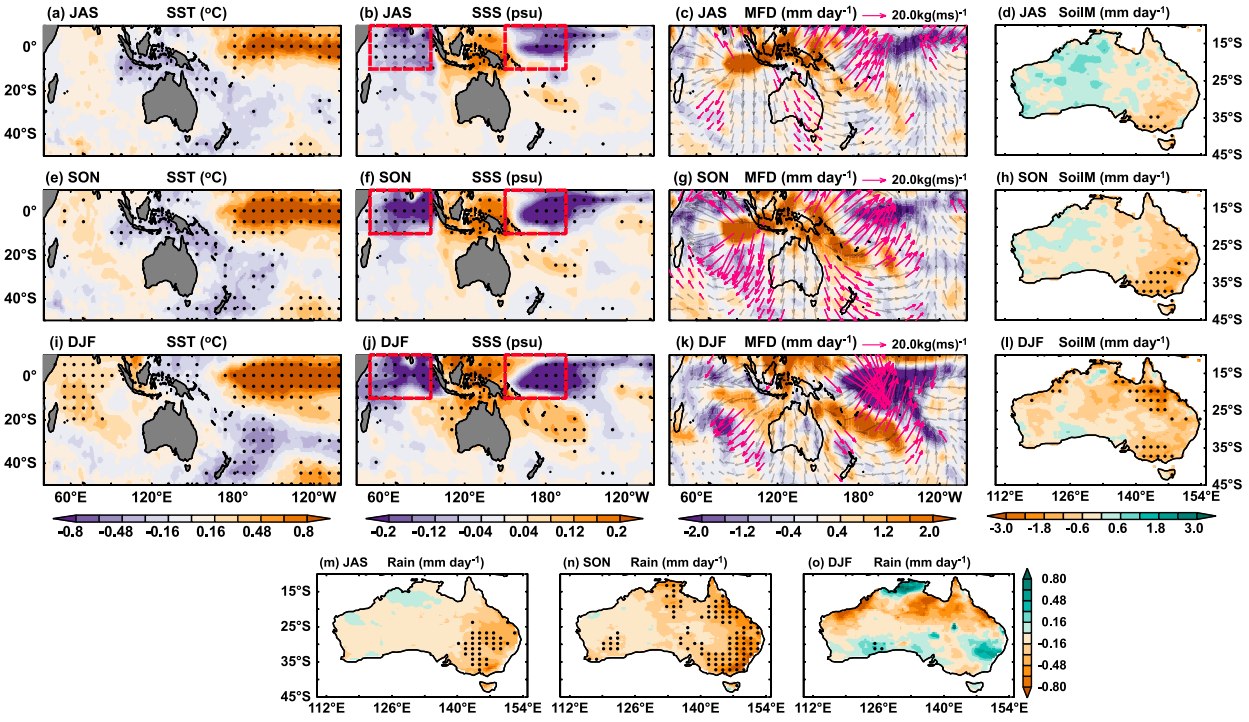

FIG. 6. As in Fig. 3, but for low SON SSS events for the SSSI region.

The presence of diverging anomalies of atmospheric moisture transport over Australia results in anomalously dry conditions with negative soil moisture anomalies (Fig. 4, fourth column). From JAS to DJF, the significantly negative soil moisture anomalies are primarily confined to eastern Australia (Fig. 4, fourth column) and this is corroborated from the rainfall anomalies (Figs. 4m–o). Similar to Figs. 3m–o, it is interesting to note that the widespread dryness during JAS (Fig. 4m) and SON (Fig. 4n) is reduced south of 25°S during DJF and concentrated over northeastern Australia (Fig. 4o). It is worth mentioning that the contrast in the wet (Fig. 3o) and dry region (Fig. 4o) during DJF could be influenced by the diversity of ENSO and IOD events (Santoso et al. 2017).

c. *Composite analysis based on high SSS anomaly events of the SSSI region*

The high SSS years of the SSSI region used for the composite analysis are 1969, 1976, 1981, 1986, 2001, and 2010. The composite analysis of high SSS events of the SSSI region is shown in Fig. 5. It is observed that there is a very weak and insignificant signal of nIOD present in the SST anomaly field during JAS (Fig. 5a) and SON (Fig. 5e) but diminished during DJF (Fig. 5i), which turns into an insignificant basinwide cooling. The corresponding SSS anomaly field shows a significant positive anomaly over SSSI region, which intensified from JAS to DJF (Fig. 5, second column). However, there is a relatively weak and insignificant corresponding SSS signal present in the SSSP region.

The SSSI region indicated by the positive SSS anomaly is the source of atmospheric moisture. The very weak and insignificant moisture that originates from the SSSI region converges mostly over the ocean around Java/Sumatra Island during JAS and SON and in the vicinity of western Australia during DJF and an insignificant transport over central Australia (Fig. 5, third column). This effect of moisture convergence is depicted in the soil moisture anomaly, which is anomalously wet (dry) in eastern (western) Australia during JAS (Fig. 5d) with increased soil moisture anomaly during SON (Fig. 5h) and DJF (Fig. 5l).

These variations of soil moisture anomalies (Fig. 5, fourth column) resemble the rainfall anomalies over Australia from JAS to DJF (Figs. 5m–o). The SSSI region's high SSS events show anomalously wet conditions over eastern Australia during JAS and SON (Figs. 5m,n) and over northern and central Australia during DJF (Fig. 5o). This analysis resembles pure nIOD, which is shown by Rathore et al. (2020).

d. *Composite analysis based on low SSS anomaly events of SSSI region*

The low SSS years of the SSSI region used for the composite analysis are 1962, 1963, 1967, 1968, 1978, and 1997. The composite analysis based on low SSS events of the SSSI region (Fig. 6) resembles the low SSS events of the SSSP region (Fig. 4). The composite mean of SST anomaly (Fig. 6, first column) shows similar features to the SSSP region (Fig. 4, first column) of co-occurring El Niño and pIOD events with significantly intense SSS anomaly over the SSSP and SSSI regions (Fig. 6, second column). Fresh (salty) anomalies around the Maritime Continent to the north of Australia indicate a sink (source) of atmospheric moisture.

The moisture originating from the salty region coincides with the atmospheric divergence and is transported toward the SSSI, the SSSP region (north of 10°S), and the Australian

continent (south of 10°S). The moisture transported toward the SSSI and SSSP regions precipitates as a result of the presence of atmospheric convergence (Fig. 6, third column) and makes these regions anomalously fresher (Fig. 6, second column). In contrast, the portion of moisture that is directed toward the Australian continent coincides with weak atmospheric convergence and results in weak anomalous wet conditions over Australia (Fig. 6, third column).

It is interesting to see that the anomalous dryness in the soil moisture (Fig. 6, fourth column) is not as pronounced as in the low SSS events of the SSSP region (Fig. 4, fourth column). In the previous case (Fig. 4, fourth column), there is a widespread anomalous dryness in the soil moisture from JAS to DJF. In contrast, the dryness is primarily concentrated over eastern Australia in the latter case (Fig. 6, fourth column). The rainfall pattern (Figs. 4m–o and 6m–o) shows a similar distribution of rainfall anomaly over Australia but with larger magnitudes in Figs. 4m–o. These differences between the precipitation and soil moisture may result from the initial state of soil moisture in JAS and may be due to the differences in evaporation over land from JAS to DJF.

In the above composite analyses, we show the physical link between the SSS, the moisture transport from the source regions, and rainfall over Australia. It is also observed that the phenomena of ENSO and IOD modulate the relationships between SSS and Australian rainfall via atmospheric moisture transport. Some of these relationships between SSS and Australian rainfall during ENSO/IOD events were also shown by Rathore et al. (2020). In the following section, we demonstrate the use of SSS, along with SST-based ENSO and IOD indices, as an additional precursor for Australian rainfall. We apply this method specifically to the Brisbane region (144°–154°E, 34°–24°S).

5. Predictability of northeast Australian rainfall using SSS

In the previous section, we established a physical link between the SSS and Australian rainfall using moisture transport in the atmosphere, SSS anomalies in the oceanic source region, and rainfall anomalies over Australia. We have also observed that the SSS values of the Indo-Pacific warm pool region in the prior season (JAS and SON) covary (and are linked by moisture transport) with the Australian rainfall in the summer season (DJF). Hence, the signal in the SSS and other variables (ENSO, IOD, and soil moisture) of the prior season can be used to assess the quality of the prediction of rainfall over the northeastern Australia and Brisbane regions.

We used the random-forest regression technique in various combinations for predicting the northeast Australian rainfall during DJF by using predictors from prior seasons (JAS and SON): 1) prediction based on ENSO and IOD indices; 2) prediction based on ENSO, IOD, and SSS; 3) prediction based on ENSO, IOD, and soil moisture; and 4) prediction based on ENSO, IOD, soil moisture, and SSS. In Fig. 7, the upper panel shows that the variance explained by the predicted time series of DJF rainfall over northeastern Australia from ENSO and IOD is $R^2 = 0.33$ (JAS). The explained variance increases to $R^2 = 0.36$ or $R^2 = 0.39$ (JAS) by including soil moisture or SSS respectively. This shows that during JAS, SSS is more important than soil moisture for the prediction of DJF rainfall. Using all the indices together the explained variance is $R^2 = 0.42$, showing, in this case, that all of the indices contribute to the prediction.

During SON (Fig. 7, lower panel), the explained variance from the combination of ENSO and IOD is $R^2 = 0.29$ and is reduced as compared with JAS ($R^2 = 0.33$). The reduction in the explained variance of the ENSO and IOD in this season compensated with a gain in the explained variance by using SSS ($R^2 = 0.42$) and soil moisture ($R^2 = 0.45$). It is also interesting to see that in contrast to JAS, during SON, the soil moisture can explain more variance when used with ENSO and IOD as compared to SSS. This suggests that during SON, soil moisture is more important than SSS for the prediction of DJF rainfall. On using all the SON indices together, the explained variance is increased to $R^2 = 0.51$ as compared with $R^2 = 0.42$ by using JAS indices for the prediction of DJF rainfall over northeastern Australia.

The improvement in the explained variance is significant at 95% confidence using a two-sample Student's t test. However, the predicted time series of different combinations of indices do not differ much from each other in high rainfall events but increase marginally in other lower rainfall years. These results show that combining the soil moisture and SSS with ENSO and IOD strongly influences the prediction of DJF rainfall over northeastern Australia with certain predictability two seasons ahead.

The importance of different indices for the prediction of DJF rainfall over northeastern Australia is further investigated in Fig. 8. This shows that among JAS indices (Fig. 8, upper panel), ENSO (Niño-3.4) has the highest importance, followed by the SSSP index and soil moisture. The SSSI index has the least importance. The soil moisture is also the index with highest importance among the SON indices (Fig. 8, lower panel) but it does not differ much in importance from the ENSO and SSSP. The memory of the soil to retain the moisture from the previous season (i.e., SON) provides improved prediction. The improved prediction, plausibly caused by feedback in the SON season that amplifies its response to the rainfall (Yu and Notaro 2020), might be the reason for the increased importance of the soil moisture in SON as compared to JAS. The indices' ranking with the explained variance suggests that most of the variability in the DJF rainfall of northeastern Australia is attributed to ENSO; however, the addition of SSS and local soil moisture indices contributes to further improvement in the prediction of rainfall.

6. Predictability of Brisbane region rainfall using SSS

Brisbane is vulnerable to flood, as demonstrated by the severe and costly floods in 1973/74 and 2010/11. Hence it is necessary to improve rainfall prediction to anticipate potential economic damage from heavy rainfall events. Here, we advocate using SSS (and soil moisture) as an additional precursor to be considered for the improvement in the prediction of rainfall over Australia.

For Brisbane rainfall prediction analysis, we have considered the DJF rainfall over the region of 144°–154°E, 34°–24°S,

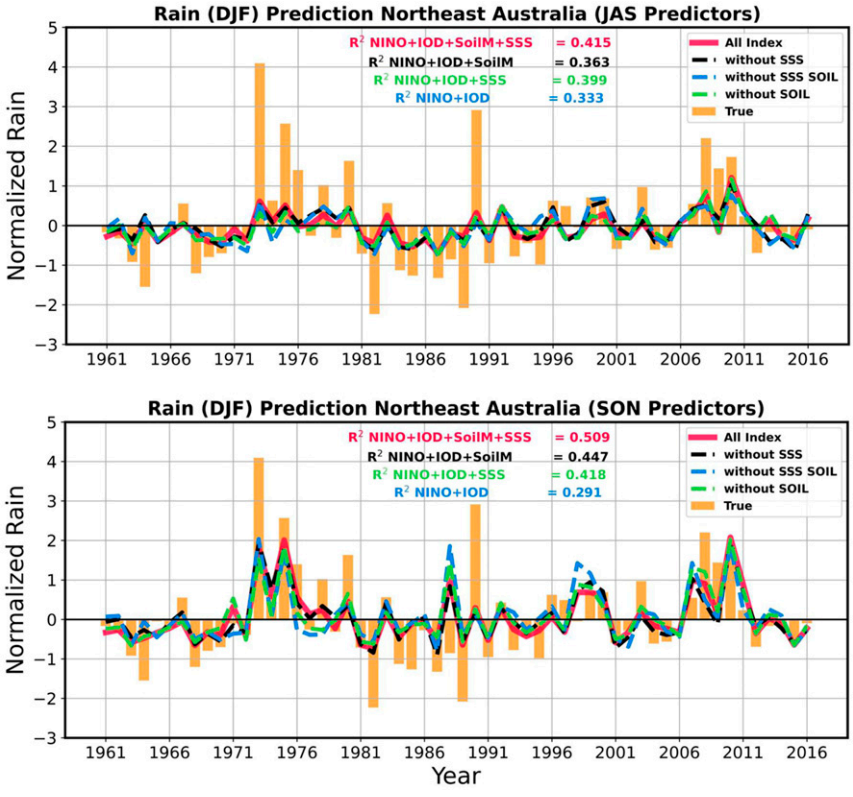

FIG. 7. Normalized time series of DJF rainfall over northeastern Australia (130°–152°E, 25°S–0°) (yellow; identical in both panels) and predicted rainfall time series by incorporating the (top) JAS and (bottom) SON indices of SSSP, SSSI, Niño-3.4, DMI, and soil moisture over northeastern Australia as predictors (red); predicted rainfall including all of the predictors except SSSP and SSSI (black); predicted rainfall including all of the predictors except soil moisture (green); and predicted rainfall without incorporating SSSP, SSSI, and soil moisture indices (blue). The variance explained by the prediction model is shown as the R^2 value.

along with the JAS and SON indices. From the random-forest regression analysis (Fig. 9, upper panel), we have found that ENSO and IOD during JAS can explain 37% ($R^2 = 0.37$) of the variance but a significant improvement is observed when combined with SSS ($R^2 = 0.51$). In comparison with SSS, the local soil moisture of Brisbane, when combined with ENSO and IOD, can explain 41% ($R^2 = 0.41$) of the variance. By combining all four indices of JAS, the predicted DJF rainfall can explain 52% ($R^2 = 0.52$) of the variance.

Similarly, when using SON predictors (Fig. 9, lower panel), ENSO and IOD can explain 36% ($R^2 = 0.36$) of variance, which is further improved to 46% ($R^2 = 0.46$) when combined with SSS. The local soil moisture, when combined with ENSO and IOD, also improves the explained variance ($R^2 = 0.39$) but less than for SSS. In contrast to JAS indices with $R^2 = 0.52$ when all the indices are combined, the variance explained using SON indices is $R^2 = 0.45$. This can be explained with the reduction in variance explained using SON SSS ($R^2 = 0.46$) as compared with the longer lead time SSS ($R^2 = 0.51$; JAS). It is also observed that, unlike northeastern Australia, the prediction of Brisbane rainfall is less affected by the local soil moisture as compared with SSS, and thus SSS is more important than the local soil moisture for the prediction of DJF rainfall over the Brisbane region.

This effect is shown in Fig. 10, where ENSO is the most important index for the prediction of DJF rainfall, followed by the rest of the indices used. For JAS, the SSSP index is the second most important index after the Niño-3.4 index, followed by IOD and SSSI (Fig. 10, upper panel). For the SON indices, the Niño-3.4 index is still of the highest importance. However, the importance factor of the SSSP index is reduced because of the increased importance of IOD during SON. This increase in the importance of IOD during SON (Fig. 10, lower panel) is likely due to weaker SSSP variability during SON or due to the ocean advection and mixing, which also explains the lower variance of DJF rainfall predicted using SON SSS. It is worth mentioning that the increased importance of IOD during SON is plausibly due to its peak occurring at this time, whereas ENSO is transitioning to attain its peak state during DJF. Interestingly, the effect of soil moisture over a smaller region like Brisbane is not as pronounced as it is for a larger and relatively dryer region like northeastern Australia. These factors combined can explain the reduced importance of the SSSP index during SON.

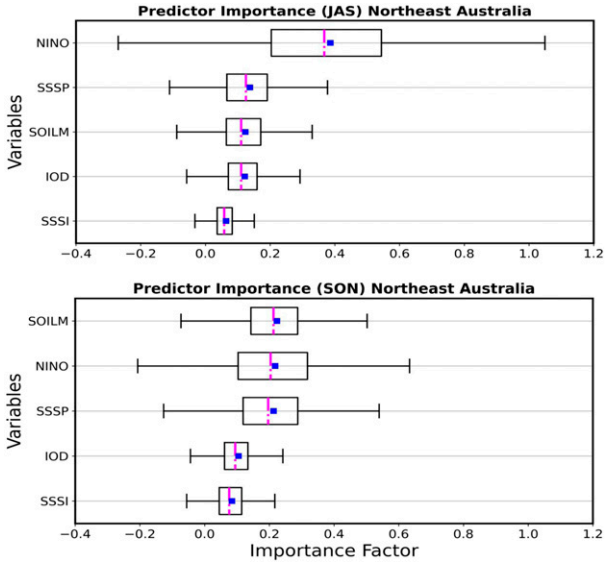

FIG. 8. Importance of predictors during (top) JAS and (bottom) SON in predicting the DJF rainfall over northeastern Australia. The magenta line is the median, and the blue square is the mean.

From the above analysis, local soil moisture, ENSO, and SSSP are the important factors for predicting DJF rainfall over northeastern Australia whereas ENSO, SSSP, and IOD are important for the Brisbane region. Apart from the conventional SST-based indices and local soil moisture, the inclusion of the SSS (the SSSP index in particular) can improve the prediction of Australian rainfall. Moreover, we have also observed that the SSS of the Indo-Pacific warm pool leads the rainfall over Australia by 3–4 months. The moisture originating from this region of anomalously high SSS eventually converges elsewhere (on ocean and land) through atmospheric moisture transport.

7. Discussion

A recent study demonstrated the link between SSS and Australian rainfall during ENSO and IOD years (Rathore et al. 2020); however, the application of SSS as a precursor of Australian rainfall was not adequately addressed. This study focuses on the use of SSS as an additional precursor for DJF rainfall over northeastern Australia and the Brisbane region. In this study, the SVD analysis (Fig. 2) shows that the SSS of the equatorial Indian Ocean (50°–95°E and 10°S–10°N) and western Pacific (150°E–165°W, 10°S–10°N) covary with the rainfall over northeastern Australia (132°–152°E, 25°–10°S) and also with other regions such as the northwestern coastal strip and the eastern seaboard region of Australia.

The signature of positive SSS in the western Pacific is quite prominent from JAS to DJF (Figs. 2a,d,g). However, positive SSS in the southwestern equatorial Indian Ocean is quite weak during JAS (Fig. 2a). It appears as a dipole anomaly, which would lead to a near-zero SSS anomaly when averaged over the region. In the following season (SON), the SSS anomaly over

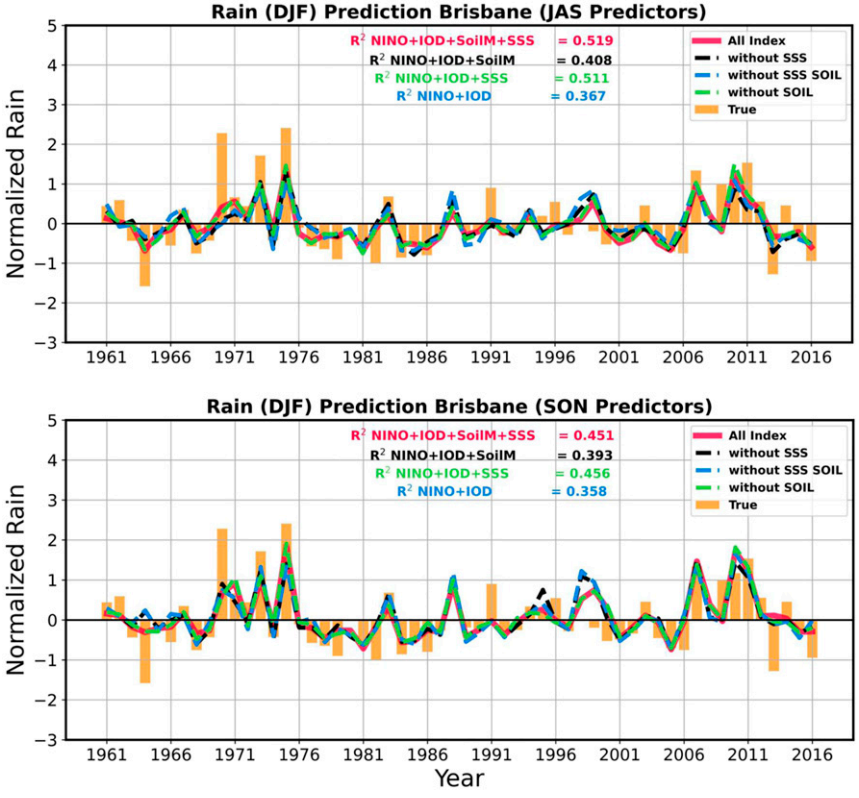

FIG. 9. As in Fig. 7, but over the broader Brisbane region (144°–154°E, 34°–24°S).

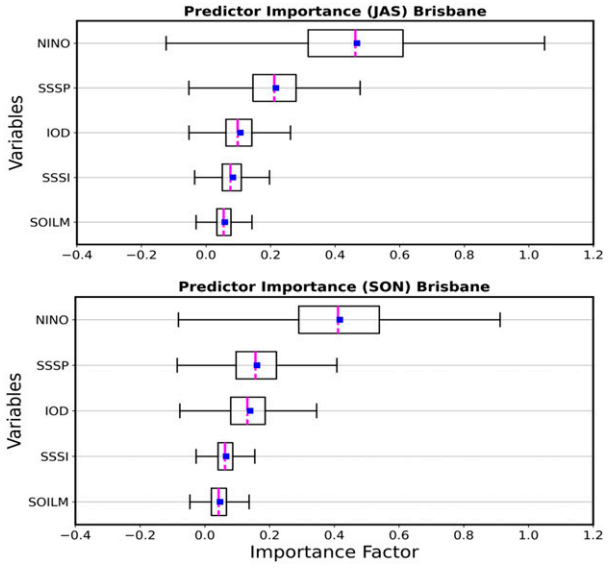

FIG. 10. As in Fig. 8, but over the broader Brisbane region. The magenta line is the median and the blue square is the mean.

the SSSI region is slightly strengthened but still weaker in comparison to the SSSP region (Fig. 2d). This low magnitude of SSS anomaly in the SSSI region may be partly responsible for its small contribution to the prediction skill. This suggests that the evolution of SSS, particularly of the SSSP region, leads the DJF rainfall over Australia.

The composite analysis of high SSS events of the SSSP and SSSI region shows the signature of co-occurring La Niña and nIOD events (Figs. 3a,e,i and 5a,e,i) with anomalously high SSS in the Indo-Pacific warm pool region (Figs. 3b,f,j and 5b,f,j). The regions of high (low) SSS broadly coincide with the regions of moisture flux divergence (convergence) in the atmosphere and represent a source (sink) of moisture for evaporation (precipitation) (Figs. 3c,g,k and 5c,g,k). It is worth mentioning that variability at the synoptic scale along with the local thermodynamic instabilities over land (Hendon et al. 1989) during the high SSS events will draw the moisture originating from the ocean surface (Figs. 3c,g,k and 5c,g,k). The anomalous moisture transport associated with the thermodynamic instabilities over land strengthens the mean moisture supply (Fig. 1) and results in anomalously wet conditions over Australia.

The presence of these thermodynamic instabilities also influences the available moisture content of the soil. Previous studies have recognized the land–atmosphere coupling via soil moisture that modulates the terrestrial precipitation (Timbal et al. 2002; Evans et al. 2011; Yu and Notaro 2020) in Australia. The presence of soil moisture also maintains the in-phase relationship of ENSO and Australian rainfall. The positive soil moisture anomalies in the presence of thermodynamic instabilities moisten the lower atmosphere, which will become unstable due to the release of latent heat by evaporation. This will further increase the moisture transport and could result in convective precipitation (Timbal et al. 2002; Evans et al. 2011). In contrast, the presence of negative soil moisture anomalies corresponds to the dry conditions over land. A detailed diagnosis of the role of soil moisture can be done by using idealized general circulation model experiments where soil moisture can be artificially controlled as in Timbal et al. (2002).

It is also important to mention that while the atmospheric transport responds rapidly to the SST (on the order of days), the synoptic ocean–atmosphere conditions may persist over longer time scales Hendon et al. (1989). Our study, along with Hendon et al. (1989), shows that the persistence of equatorial Pacific and Indian Ocean large-scale atmosphere–ocean phenomena (e.g., ENSO and IOD) drives the land anomalies (anomalies of rainfall and soil moisture) and their persistence. Also, the phase of these large-scale drivers and their persistence affects the evolution and intensity of the northeast Australian monsoon. The detailed diagnosis of these synoptic-scale coupled ocean and atmosphere conditions is beyond the scope of this study. However, we acknowledge that the persistence of these synoptic conditions over a longer period can generate a leading response in various land, oceanic, and atmospheric fields. Hence, in this study we use the leading responses of ENSO, IOD, SSS, and soil moisture from prior seasons (JAS and SON) to assist the prediction of Australian rainfall for the following season (DJF).

Therefore, during the high SSS events of the SSSP and SSSI regions, the presence of positive soil moisture anomalies during JAS and SON (Figs. 3d,h,l and 5d,h,l) corroborates anomalously wet conditions over Australia (Figs. 3m–o and 5m–o). This coupling between the soil moisture and the atmospheric circulation, along with the albedo and vegetation effects, contributes to the enhancement of rainfall over land (Evans et al. 2017).

In contrast, the composite analysis of low SSS events in the SSSP and SSSI regions shows the signature of co-occurring El Niño and pIOD events (Figs. 4a,e,i and 6a,e,i) with anomalously low SSS in the Indo-Pacific warm pool region (Figs. 4b,f,j and 6b,f,j). The moisture originates from north of Australia and leaves an imprint of anomalously high SSS that broadly coincides with the anomalously high MFD (Figs. 4c,g,k and 6c,g,k). Unlike the high SSS events of the SSSP and SSSI regions, the moisture flux originating from the ocean surface during low SSS events (Figs. 4c,g,k and 6c,g,k) weakens the mean moisture supply (Fig. 1) and results in anomalously dry conditions over Australia.

Although the moisture transport is directed toward Australia, it coincides with atmospheric divergence and negative soil moisture anomaly (Figs. 4d,h,l and 6d,h,l). These conditions combine to result in anomalously dry conditions over northeastern Australia (Figs. 4m and 6m). The identification of physical mechanisms and links between oceanic, atmospheric, and land variables leads to greater predictive skills for Australian rainfall. We have also performed a composite analysis based on high and low rainfall events over northeastern Australia (figure not shown). We have found that the composite mean based on high and low rainfall events is broadly similar but with different magnitudes to the composite analysis performed in Figs. 3–6, which are based on high and low SSS events. This analysis suggests that the SSS variation is a cleaner indicator for the atmospheric moisture

transport and terrestrial precipitation than compositing of high or low rainfall events.

As previous studies have shown, Australian rainfall is strongly modulated by the variability of the tropical Indian and Pacific Ocean climate associated with ENSO and IOD events (Risbey et al. 2009; Ummenhofer et al. 2009; Cai et al. 2011). In this study, we bring a new perspective of using SSS as an additional precursor for improving the prediction of Australian rainfall. For the prediction of DJF rainfall over northeastern Australia and the Brisbane region, we used random-forest regression analysis in which we used SSS of Indo-Pacific warm pool region as an additional precursor, along with the local soil moisture, Niño-3.4 index, and DMI to represents the ENSO and IOD phenomena. We found that the prediction of the DJF rainfall over northeastern Australia (Fig. 7) and the Brisbane region (Fig. 9) is improved by the addition of SSS of SSSP and SSSI regions along with the local soil moisture, ENSO, and IOD indices.

Unlike other studies (Li et al. 2016b; Chen et al. 2019), we have shown (Figs. 7 and 9) in our analysis that most of the high rainfall events are well captured even without including SSS and local soil moisture. The plausible reason for this is the location of Australia and its monsoon season (DJF). Northeastern Australia is quite close to the equator and particularly to the western equatorial Pacific, which is highly influenced by equatorial dynamics predominantly through ENSO (Rathore et al. 2020). Moreover, the Australian monsoon season (DJF) is also the season when ENSO matures and attains its peak. In fact, ENSO starts to evolve from JJA and intensifies in the following seasons until February of the following year and decays thereafter (Jong et al. 2020). Hence, most of the variance (Figs. 7 and 9) in DJF rainfall of Australia can be strongly attributed to the ENSO dynamics (Zhao et al. 2019). We have also tested our analysis by including the SON rainfall of the SSSP region as a predictor along with all the indices used in the above analysis. We have found that the rainfall over the ocean in the SSSP region has limited impact on the prediction of DJF rainfall over northeastern Australia (figure not shown).

Our result differs from those of Li et al. (2016b) and Chen et al. (2019), where SSS was the most important predictor, whereas in this study local soil moisture is the most important predictor followed by ENSO and SSSP (Fig. 7, lower panel). By adding the soil moisture index of northeastern Australia along with ENSO and IOD indices, the explained variance of DJF rainfall is increased from 29% to 45%, which is 3% higher than that when SSS is combined with ENSO and IOD. The explained variance of 51% is observed by combining SSS and soil moisture with the ENSO and IOD indices. The additional gain of 21% in the explained variance is achieved by including local soil moisture of northeastern Australia and remote SSS (SSSP). This suggests that for the prediction of DJF rainfall over northeastern Australia, the local soil moisture and SSS from prior seasons are also important precursors. It is worth mentioning that unlike northeastern Australia, where local soil moisture plays a crucial role (Fig. 8), in the Brisbane region the local soil moisture is of least importance and ENSO, SSSP, and IOD are of highest importance (Fig. 10). Our study suggests that the prediction of rainfall over northeastern Australia and the broader Brisbane region can be improved by including SSS along with other conventional indices such as ENSO, IOD, and local soil moisture.

It is important to mention that the SSS does not shape the rainfall over land. In fact, the SSS anomaly is the balance between the evaporation and precipitation (E minus P). The moisture that originates from the ocean surface to precipitate elsewhere leaves an imprint on the SSS. This region of anomalously high SSS marks a source of atmospheric moisture and is also associated with the region of moisture flux divergence in the atmosphere. However, the convergence of atmospheric moisture over land for precipitation depends on the synoptic-scale variability as well as on the local thermodynamic instabilities over land. Hence, our study does not suggest that the SSS is a dynamically active variable that drives or shapes the precipitation over land; it is rather a passive variable. In fact, it is an imprint of the moisture exchange process between the ocean and atmosphere that can be used to monitor the downstream terrestrial precipitation and to improve prediction.

Our study also suggests that the persistent signals of ENSO evolution and the response in soil moisture due to convergence/divergence from JAS to SON are the dominant drivers for the precipitation over northeastern Australia during DJF. The prediction of Australian rainfall can be improved by tracking the ENSO signature in SST and/or SSS anomalies. Hackert et al. (2019) have shown that assimilating SSS, alongside the conventional parameters, in coupled models improves the overall forecast of ENSO.

It is worth mentioning that the predicted rainfall is not in one-to-one relation with the observed rainfall; there is a future scope to further improve the prediction of rainfall by including other potential predictors such as Indian Ocean basinwide mode (Dommenget 2011). Also, across the seasons IOD is the second leading mode of the Indian Ocean after the basinwide mode, but when looking only at the SON season the IOD seems to be more dominant than the basinwide mode. Hence, the seasonality of ENSO and the IOD also plays an important role in the prediction of rainfall over Australia.

It is also interesting to note that the heavy precipitation year of 1990/91 is not captured by the random-forest regression analysis whether SSS is included or not. Hence, it is worth discussing the heavy precipitation year of 1990/91 in the northeastern Australia region (Fig. 7). The reasons suggested by previous studies are heavy rainfall over the Lake Eyre basin (Pook et al. 2014) and a tropical cyclone "Joy" that dissipated south of Townsville, Queensland (Van Woesik et al. 1995; McConochie et al. 2004). During the heavy precipitation over Lake Eyre, a dominant synoptic system that combined a monsoon trough at mean sea level and a geopotential trough in the midtroposphere was responsible (Pook et al. 2014). Moreover, the tropical cyclone also brought heavy rainfall of more than 2000 mm between 23 December 1990 and 7 January 1991 over the region between Prosperine (20°S) and Rockhampton (23°S). High rainfall associated with tropical low pressure systems continued to the end of March 1991, which led to extensive flooding of the central Queensland coastal plain (Van Woesik et al. 1995).

Furthermore, this study does not account for the effect of upper ocean processes such as advection, diffusion, and vertical entrainment (Yu 2011) and the local land surface processes that influence the soil moisture–precipitation feedback mechanism, such as vegetation and albedo (Evans et al. 2017). However, because of the significant uncertainties in the estimation of evaporation minus precipitation flux ($E - P$) from the present generation reanalysis products, the SSS appears to be a strong candidate to improve the prediction of terrestrial rainfall (Yu et al. 2017).

8. Conclusions

This study demonstrates the moisture pathways of the SSSP and SSSI regions, which covary with the Australian rainfall over various regions (e.g., the northeast, the eastern seaboard, and the northwestern coastal strip). The events of anomalously high and low SSS of the SSSP and SSSI regions are connected with the phases of ENSO (La Niña and El Niño) and IOD (nIOD and pIOD) in the equatorial region of the Indo-Pacific warm pool. The moisture that originates from the SSSP and SSSI regions due to evaporation leaves an imprint on the SSS, which broadly coincides with anomalously high MFD in the atmosphere that converges elsewhere to produce precipitation.

Our study suggests that the land–atmosphere coupling may have a strong influence on the convergence and divergence of incoming atmospheric moisture toward land. As the soil moisture influences the Australian precipitation during summer (DJF), it also permits the maintenance of the in-phase ENSO–rainfall relationship (Timbal et al. 2002; Evans et al. 2011). The presence of positive soil moisture anomaly coincides with the moisture flux convergence and results in anomalously wet conditions with widespread precipitation over land. In contrast, the presence of negative soil moisture anomaly (dry land) coincides with the moisture flux divergence and results in anomalously dry conditions over land with a negative rainfall anomaly.

Our predictive analysis using a machine-learning algorithm (i.e., random-forest regression) supports the ENSO–rainfall relationship. For northeastern Australia, after local soil moisture, ENSO is the second most important precursor for predicting the Australian rainfall followed by SSSP. Unlike northeastern Australia, the local soil moisture of the Brisbane region is of least importance whereas ENSO and SSSP are of highest importance. Our study shows an improvement in the prediction of rainfall over a large region of northeastern Australia and a small region of Brisbane by the inclusion of the SSS (especially the SSSP) indices. Hence, continuous monitoring of SSS is required for the better prediction of global to regional hydroclimatic conditions.

Acknowledgments. This research is funded through the Earth System and Climate Change Hub of the Australian government's National Environmental Science Programme. The assistance of computing resources from the National Computational Infrastructure supported by the Australian Government is acknowledged. Author Ummenhofer acknowledges support from the U.S. National Science Foundation under Grant OCE-1663704. Author Feng was supported by the Centre for Southern Hemisphere Oceans Research (CSHOR), which is a joint initiative between the Qingdao National Laboratory for Marine Science and Technology (QNLM), CSIRO, University of New South Wales, and the University of Tasmania. The authors also acknowledge Dr. Manali Pal for technical discussion on machine learning.

Data availability statement. The time series of the Niño-3.4 index and dipole mode index are obtained from https://origin.cpc.ncep.noaa.gov/products/analysis_monitoring/ensostuff/ONI_v5.php and https://www.esrl.noaa.gov/psd/gcos_wgsp/Timeseries/DMI/, respectively. The SSS data are obtained from the ECMWF Ocean Reanalysis System 4 (ORAS4) (https://icdc.cen.uni-hamburg.de/daten/reanalysis-ocean/easy-init-ocean/ecmwf-ocean-reanalysis-system-4-oras4.html) and Hadley Centre subsurface objective analyses (EN4.2.1) (https://www.metoffice.gov.uk/hadobs/en4/download-en4-2-1.html) with the bias corrections from Levitus et al. (2009) and Gouretski and Reseghetti (2010). Precipitation data are obtained from the National Weather Service/Climate Prediction Center (http://apdrc.soest.hawaii.edu/las/v6/dataset?catitem=1719), Climate Research Unit (CRU TS4.04) (https://catalogue.ceda.ac.uk/), and Australian Water Availability Project. Specific humidity and horizontal winds between 1000 and 500 hPa are from NCEP–NCAR Reanalysis 1 (https://psl.noaa.gov/data/gridded/data.ncep.reanalysis.pressure.html). SST data are from HadISST1 (http://apdrc.soest.hawaii.edu/las/v6/dataset?catitem=2847). Soil moisture data are from NOAA's CPC Soil Moisture dataset (https://psl.noaa.gov/data/gridded/data.cpcsoil.html).

REFERENCES

Altmann, A., L. Toloşi, O. Sander, and T. Lengauer, 2010: Permutation importance: A corrected feature importance measure. *Bioinformatics*, **26**, 1340–1347, https://doi.org/10.1093/bioinformatics/btq134.

Ashok, K., Z. Guan, and T. Yamagata, 2003: Influence of the Indian Ocean dipole on the Australian winter rainfall. *Geophys. Res. Lett.*, **30**, 1821, https://doi.org/10.1029/2003GL017926.

Ballabrera-Poy, J., R. Murtugudde, and A. J. Busalacchi, 2002: On the potential impact of sea surface salinity observations on ENSO predictions. *J. Geophys. Res.*, **107**, 8007, https://doi.org/10.1029/2001JC000834.

Balmaseda, M. A., K. Mogensen, and A. T. Weaver, 2013: Evaluation of the ECMWF ocean reanalysis system ORAS4. *Quart. J. Roy. Meteor. Soc.*, **139**, 1132–1161, https://doi.org/10.1002/qj.2063.

Breiman, L., 2001: Random forests. *Mach. Learn.*, **45**, 5–32, https://doi.org/10.1023/A:1010933404324.

Cai, W., T. Cowan, and A. Sullivan, 2009: Recent unprecedented skewness towards positive Indian Ocean dipole occurrences and its impact on Australian rainfall. *Geophys. Res. Lett.*, **36**, L11705, https://doi.org/10.1029/2009GL037604.

——, P. van Rensch, T. Cowan, and H. H. Hendon, 2011: Teleconnection pathways of ENSO and the IOD and the mechanisms for impacts on Australian rainfall. *J. Climate*, **24**, 3910–3923, https://doi.org/10.1175/2011JCLI4129.1.

——, ——, ——, and ——, 2012: An asymmetry in the IOD and ENSO teleconnection pathway and its impact on Australian

climate. *J. Climate*, **25**, 6318–6329, https://doi.org/10.1175/JCLI-D-11-00501.1.

Chen, B., H. Qin, G. Chen, and H. Xue, 2019: Ocean salinity as a precursor of summer rainfall over the East Asian monsoon region. *J. Climate*, **32**, 5659–5676, https://doi.org/10.1175/JCLI-D-18-0756.1.

Chen, J., M. Li, and W. Wang, 2012: Statistical uncertainty estimation using random forests and its application to drought forecast. *Math. Probl. Eng.*, **2012**, 915053, https://doi.org/10.1155/2012/915053.

Chen, M., P. Xie, J. E. Janowiak, and P. H. Arkin, 2002: Global land precipitation: A 50-yr monthly analysis based on gauge observations. *J. Hydrometeor.*, **3**, 249–266, https://doi.org/10.1175/1525-7541(2002)003<0249:GLPAYM>2.0.CO;2.

Das, P., and V. Pandey, 2019: Use of logistic regression in land-cover classification with moderate-resolution multispectral data. *J. Indian Soc. Remote Sens.*, **47**, 1443–1454, https://doi.org/10.1007/S12524-019-00986-8.

Delcroix, T., C. Henin, V. Porte, and P. Arkin, 1996: Precipitation and sea-surface salinity in the tropical Pacific Ocean. *Deep-Sea Res. I*, **43**, 1123–1141, https://doi.org/10.1016/0967-0637(96)00048-9.

Dommenget, D., 2011: An objective analysis of the observed spatial structure of the tropical Indian Ocean SST variability. *Climate Dyn.*, **36**, 2129–2145, https://doi.org/10.1007/s00382-010-0787-1.

Evans, J. P., and I. Boyer-Souchet, 2012: Local sea surface temperatures add to extreme precipitation in northeast Australia during La Niña. *Geophys. Res. Lett.*, **39**, L10803, https://doi.org/10.1029/2012GL052014.

——, A. J. Pitman, and F. T. Cruz, 2011: Coupled atmospheric and land surface dynamics over southeast Australia: A review, analysis and identification of future research priorities. *Int. J. Climatol.*, **31**, 1758–1772, https://doi.org/10.1002/joc.2206.

——, X. Meng, and M. F. McCabe, 2017: Land surface albedo and vegetation feedbacks enhanced the millennium drought in south-east Australia. *Hydrol. Earth Syst. Sci.*, **21**, 409–422, https://doi.org/10.5194/hess-21-409-2017.

Fan, Y., and H. van den Dool, 2004: Climate Prediction Center global monthly soil moisture data set at 0.5° resolution for 1948 to present. *J. Geophys. Res.*, **109**, D10102, https://doi.org/10.1029/2003JD004345.

Firth, L., M. L. Hazelton, and E. P. Campbell, 2005: Predicting the onset of Australian winter rainfall by nonlinear classification. *J. Climate*, **18**, 772–781, https://doi.org/10.1175/JCLI-3291.1.

Ghosh, S. M., and M. D. Behera, 2018: Aboveground biomass estimation using multi-sensor data synergy and machine learning algorithms in a dense tropical forest. *Appl. Geogr.*, **96**, 29–40, https://doi.org/10.1016/j.apgeog.2018.05.011.

Good, S. A., M. J. Martin, and N. A. Rayner, 2013: EN4: Quality controlled ocean temperature and salinity profiles and monthly objective analyses with uncertainty estimates. *J. Geophys. Res. Oceans*, **118**, 6704–6716, https://doi.org/10.1002/2013JC009067.

Gouretski, V., and F. Reseghetti, 2010: On depth and temperature biases in bathythermograph data: Development of a new correction scheme based on analysis of a global ocean database. *Deep-Sea Res. I.* **57**, 812–833, https://doi.org/10.1016/j.dsr.2010.03.011.

Grunseich, G., B. Subrahmanyam, V. S. N. Murty, B. S. Giese, 2011: Sea surface salinity variability during the Indian Ocean Dipole and ENSO events in the tropical Indian Ocean. *J. Geophys. Res.*, **116**, C11013, https://doi.org/10.1029/2011JC007456.

Hackert, E. C., R. M. Kovach, A. J. Busalacchi, and J. Ballabrera-Poy, 2019: Impact of Aquarius and SMAP satellite sea surface salinity observations on coupled El Niño/Southern Oscillation forecasts. *J. Geophys. Res. Oceans*, **124**, 4546–4556, https://doi.org/10.1029/2019JC015130.

Halgamuge, M. N., and A. Nirmalathas, 2017: Analysis of large flood events: Based on flood data during 1985–2016 in Australia and India. *Int. J. Disaster Risk Reduct.*, **24**, 1–11, https://doi.org/10.1016/j.ijdrr.2017.05.011.

Hayes, J., and A. Goonetilleke, 2013: Building community resilience—Learning from the 2011 floods in southeast Queensland, Australia. *Eighth Annual Conf. of the International Institute for Infrastructure, Renewal and Reconstruction: Int. Conf. on Disaster Management (IIIRR 2012)*, IIIRR, 51–60, https://www.civil.kumamoto-u.ac.jp/kakimoto/iiirr/.

Hendon, H. H., N. E. Davidson, and B. Gunn, 1989: Australian summer monsoon onset during AMEX 1987. *Mon. Wea. Rev.*, **117**, 370–390, https://doi.org/10.1175/1520-0493(1989)117<0370:ASMODA>2.0.CO;2.

——, E.-P. Lim, J. M. Arblaster, and D. L. T. Anderson, 2014: Causes and predictability of the record wet east Australian spring 2010. *Climate Dyn.*, **42**, 1155–1174, https://doi.org/10.1007/s00382-013-1700-5.

Holmes, C., 2012: Queensland Floods Commission of Inquiry. Queensland Floods Commission of Inquiry Rep., 658 pp., https://www.floodcommission.qld.gov.au/publications/final-report/.

Hu, P., Q. Zhang, P. Shi, B. Chen, and J. Fang, 2018: Flood-induced mortality across the globe: Spatiotemporal pattern and influencing factors. *Sci. Total Environ.*, **643**, 171–182, https://doi.org/10.1016/J.SCITOTENV.2018.06.197.

Huang, B., and Coauthors, 2017: Extended Reconstructed Sea Surface Temperature, version 5 (ERSSTv5): Upgrades, validations, and intercomparisons. *J. Climate*, **30**, 8179–8205, https://doi.org/10.1175/JCLI-D-16-0836.1.

Jong, B. T., M. Ting, R. Seager, and W. B. Anderson, 2020: ENSO teleconnections and impacts on U.S. summertime temperature during a multiyear La Niña life cycle. *J. Climate*, **33**, 6009–6024, https://doi.org/10.1175/JCLI-D-19-0701.1.

Kalnay, E., and Coauthors, 1996: The NCEP/NCAR 40-Year Reanalysis Project. *Bull. Amer. Meteor. Soc.*, **77**, 437–471, https://doi.org/10.1175/1520-0477(1996)077<0437:TNYRP>2.0.CO;2.

Kido, S., T. Tozuka, and W. Han, 2019: Anatomy of salinity anomalies associated with the positive Indian Ocean dipole. *J. Geophys. Res. Oceans*, **124**, 8116–8139, https://doi.org/10.1029/2019JC015163.

King, A. D., M. G. Donat, L. V. Alexander, and D. J. Karoly, 2015: The ENSO-Australian rainfall teleconnection in reanalysis and CMIP5. *Climate Dyn.*, **44**, 2623–2635, https://doi.org/10.1007/s00382-014-2159-8.

Levitus, S., J. I. Antonov, T. P. Boyer, R. A. Locarnini, H. E. Garcia, and A. V. Mishonov, 2009: Global ocean heat content 1955–2008 in light of recently revealed instrumentation problems. *Geophys. Res. Lett.*, **36**, L07608, https://doi.org/10.1029/2008GL037155.

Li, L., W. Li, and A. P. Barros, 2013: Atmospheric moisture budget and its regulation of the summer precipitation variability over the southeastern United States. *Climate Dyn.*, **41**, 613–631, https://doi.org/10.1007/s00382-013-1697-9.

——, R. W. Schmitt, C. C. Ummenhofer, and K. B. Karnauskas, 2016a: Implications of North Atlantic sea surface salinity for

summer precipitation over the U.S. Midwest: Mechanisms and predictive value. *J. Climate*, **29**, 3143–3159, https://doi.org/10.1175/JCLI-D-15-0520.1.

——, ——, ——, and ——, 2016b: North Atlantic salinity as a predictor of Sahel rainfall. *Sci. Adv.*, **2**, e1501588, https://doi.org/10.1126/sciadv.1501588.

Lim, E. P., and H. H. Hendon, 2015: Understanding and predicting the strong southern annular mode and its impact on the record wet east Australian spring 2010. *Climate Dyn.*, **44**, 2807–2824, https://doi.org/10.1007/s00382-014-2400-5.

Lynch, P., 1988: Deducing the wind from vorticity and divergence. *Mon. Wea. Rev.*, **116**, 86–93, https://doi.org/10.1175/1520-0493(1988)116<0086:DTWFVA>2.0.CO;2.

McBride, J. L., and N. Nicholls, 1983: Seasonal relationships between Australian rainfall and the Southern Oscillation. *Mon. Wea. Rev.*, **111**, 1998–2004, https://doi.org/10.1175/1520-0493(1983)111<1998:SRBARA>2.0.CO;2.

McConochie, J. D., T. A. Hardy, and L. B. Mason, 2004: Modelling tropical cyclone over-water wind and pressure fields. *Ocean Eng.*, **31**, 1757–1782, https://doi.org/10.1016/j.oceaneng.2004.03.009.

Mitchell, T. D., and P. D. Jones, 2005: An improved method of constructing a database of monthly climate observations and associated high-resolution grids. *Int. J. Climatol.*, **25**, 693–712, https://doi.org/10.1002/joc.1181.

Mogensen, K., M. Alonso, and A. Weaver, 2012: The NEMOVAR ocean data assimilation system as implemented in the ECMWF ocean analysis for System 4. ECMWF Tech. Memo. 668, 59 pp., https://www.ecmwf.int/sites/default/files/elibrary/2012/11174-nemovar-ocean-data-assimilation-system-implemented-ecmwf-ocean-analysis-system-4.pdf.

NCCARF, 2012: Protecting structures from floodwater. NCCARF Fact Sheet FS-2/2012, 2 pp., https://nccarf.edu.au/wp-content/uploads/2019/03/ProtectingStructuresfromFloodwater-factsheet_0.pdf.

New, M., M. Hulme, and P. Jones, 2000: Representing twentieth-century space–time climate variability. Part II: Development of 1901-96 monthly grids of terrestrial surface climate. *J. Climate*, **13**, 2217–2238, https://doi.org/10.1175/1520-0442(2000)013<2217:RTCSTC>2.0.CO;2.

Nicholls, N., 2001: Commentary and analysis: The insignificance of significance testing. *Bull. Amer. Meteor. Soc.*, **82**, 981–986, https://doi.org/10.1175/1520-0477(2001)082<0981:CAATIO>2.3.CO;2.

Noi, P. T., J. Degener, and M. Kappas, 2017: Comparison of multiple linear regression, cubist regression, and random forest algorithms to estimate daily air surface temperature from dynamic combinations of MODIS LST data. *Remote Sens.*, **9**, 398, https://doi.org/10.3390/rs9050398.

Pal, M., J. V. Ratnam, M. Nonaka, and S. K. Behera, 2020: Long-lead prediction of ENSO Modoki index using machine learning algorithms. *Sci. Rep.*, **10**, 365, https://doi.org/10.1038/s41598-019-57183-3.

Pook, M. J., J. S. Risbey, C. C. Ummenhofer, P. R. Briggs, and T. J. Cohen, 2014: A synoptic climatology of heavy rain events in the Lake Eyre and Lake Frome catchments. *Front. Environ. Sci.*, **2**, 1–8, https://doi.org/10.3389/fenvs.2014.00054.

Power, S., and Coauthors, 1998: Australian temperature, Australian rainfall and the Southern Oscillation, 1910–1992: Coherent variability and recent changes. *Aust. Meteor. Mag.*, **47**, 85–101.

——, F. Tseitkin, V. Mehta, B. Lavery, S. Torok, and N. Holbrook, 1999: Decadal climate variability in Australia during the twentieth century. *Int. J. Climatol.*, **19**, 169–184, https://doi.org/10.1002/(SICI)1097-0088(199902)19:2<169::AID-JOC356>3.0.CO;2-Y.

——, M. Haylock, R. Colman, and X. Wang, 2006: The predictability of interdecadal changes in ENSO activity and ENSO teleconnections. *J. Climate*, **19**, 4755–4771, https://doi.org/10.1175/JCLI3868.1.

Rathore, S., N. L. Bindoff, C. C. Ummenhofer, H. E. Phillips, and M. Feng, 2020: Near-surface salinity reveals the oceanic sources of moisture for Australian precipitation through atmospheric moisture transport. *J. Climate*, **33**, 6707–6730, https://doi.org/10.1175/JCLI-D-19-0579.1.

Raupach, M. R., P. R. Briggs, V. Haverd, E. A. King, M. Paget, and C. M. Trudinger, 2009: Australian Water Availability Project (AWAP): CSIRO Marine and Atmospheric Research component: Final report for Phase 3. Centre for Australian Weather and Climate Research CAWCR Tech. Rep. 013, 67 pp., http://www.csiro.au/awap/doc/CTR_013_online_FINAL.pdf.

Rayner, N. A., and Coauthors, 2003: Global analyses of sea surface temperature, sea ice, and night marine air temperature since the late nineteenth century. *J. Geophys. Res.*, **108**, 4407, https://doi.org/10.1029/2002JD002670.

Risbey, J. S., M. J. Pook, P. C. Mclntosh, M. C. Wheeler, and H. H. Hendon, 2009: On the remote drivers of rainfall variability in Australia. *Mon. Wea. Rev.*, **137**, 3233–3253, https://doi.org/10.1175/2009MWR2861.1.

Saji, N. H., B. N. Goswami, P. N. Vinayachandran, and T. Yamagata, 1999: A dipole mode in the tropical Indian Ocean. *Nature*, **401**, 360–363, https://doi.org/10.1038/43854.

Santoso, A., M. J. McPhaden, and W. Cai, 2017: The defining characteristics of ENSO extremes and the strong 2015/2016 El Niño. *Rev. Geophys.*, **55**, 1079–1129, https://doi.org/10.1002/2017RG000560.

Seager, R., and N. Henderson, 2013: Diagnostic computation of moisture budgets in the ERA-Interim reanalysis with reference to analysis of CMIP-archived atmospheric model data. *J. Climate*, **26**, 7876–7901, https://doi.org/10.1175/JCLI-D-13-00018.1.

Singh, A., and T. Delcroix, 2011: Estimating the effects of ENSO upon the observed freshening trends of the western tropical Pacific Ocean. *Geophys. Res. Lett.*, **38**, L21607, https://doi.org/10.1029/2011GL049636.

Taschetto, A. S., A. S. Gupta, H. H. Hendon, C. C. Ummenhofer, and M. H. England, 2011: The contribution of Indian Ocean sea surface temperature anomalies on Australian summer rainfall during El Niño events. *J. Climate*, **24**, 3734–3747, https://doi.org/10.1175/2011JCLI3885.1.

Terray, P., P. Delecluse, S. Labattu, and L. Terray, 2003: Sea surface temperature associations with the late Indian summer monsoon. *Climate Dyn.*, **21**, 593–618, https://doi.org/10.1007/s00382-003-0354-0.

Timbal, B., S. Power, R. Colman, J. Viviand, and S. Lirola, 2002: Does soil moisture influence climate variability and predictability over Australia? *J. Climate*, **15**, 1230–1238, https://doi.org/10.1175/1520-0442(2002)015<1230:DSMICV>2.0.CO;2.

Ummenhofer, C. C., M. H. England, P. C. Mclntosh, G. A. Meyers, M. J. Pook, J. M. Risbey, A. S. Gupta, and A. S. Taschetto, 2009: What causes southeast Australia's worst droughts? *Geophys. Res. Lett.*, **36**, L04706, https://doi.org/10.1029/2008GL036801.

——, and Coauthors, 2011: Indian and Pacific Ocean influences on southeast Australian drought and soil moisture. *J. Climate*, **24**, 1313–1336, https://doi.org/10.1175/2010JCLI3475.1.

——, A. S. Gupta, M. H. England, A. S. Taschetto, P. R. Briggs, and M. R. Raupach, 2015: How did ocean warming affect

Australian rainfall extremes during the 2010/2011 La Niña event? *Geophys. Res. Lett.*, **42**, 9942–9951, https://doi.org/10.1002/2015GL065948.

Van Woesik, R., L. M. De Vantier, and J. S. Glazebrook, 1995: Effects of cyclone "Joy" on nearshore coral communities of the Great Barrier Reef. *Mar. Ecol. Prog. Ser.*, **128**, 261–270, https://doi.org/10.3354/meps128261.

Wallace, J. M., C. Smith, and C. S. Bretherton, 1992: Singular value decomposition of wintertime sea surface temperature and 500-mb height anomalies. *J. Climate*, **5**, 561–576, https://doi.org/10.1175/1520-0442(1992)005<0561:SVDOWS>2.0.CO;2.

Yu, L., 2011: A global relationship between the ocean water cycle and near-surface salinity. *J. Geophys. Res.*, **116**, C10025, https://doi.org/10.1029/2010JC006937.

——, X. Jin, S. A. Josey, T. Lee, A. Kumar, C. Wen, and Y. Xue, 2017: The global ocean water cycle in atmospheric reanalysis, satellite, and ocean salinity. *J. Climate*, **30**, 3829–3852, https://doi.org/10.1175/JCLI-D-16-0479.1.

Yu, Y., and M. Notaro, 2020: Observed land surface feedbacks on the Australian monsoon system. *Climate Dyn.*, **54**, 3021–3040, https://doi.org/10.1007/S00382-020-05154-0.

Yuan, C., and T. Yamagata, 2015: Impacts of IOD, ENSO and ENSO Modoki on the Australian winter wheat yields in recent decades. *Sci. Rep.*, **5**, 17252, https://doi.org/10.1038/srep17252.

Zhao, M., H. Zhang, and I. Dharssi, 2019: On the soil moisture memory and influence on coupled seasonal forecasts over Australia. *Climate Dyn.*, **52**, 7085–7109, https://doi.org/10.1007/S00382-018-4566-8.

Zhou, T. J., and R. C. Yu, 2005: Atmospheric water vapor transport associated with typical anomalous summer rainfall patterns in China. *J. Geophys. Res.*, **110**, D08104, https://doi.org/10.1029/2004JD005413.

Zhu, Z., 2018: Breakdown of the relationship between Australian summer rainfall and ENSO caused by tropical Indian Ocean SST warming. *J. Climate*, **31**, 2321–2336, https://doi.org/10.1175/JCLI-D-17-0132.1.